856

A STUDY OF THE "LD-4 REGENERATOR" SAMPLING MECHANISM

by

STEPHEN J.G. BROWN

Introduction

This project concerns the LD-4 regenerator which forms the basis of a long haul digital communications line operating at a bit rate of 280 Megabits per second. One of the problems associated with the regenerator occurs within the sampling mechanism. If one samples the incoming deteriorated signal well below the voltage threshold*, the regenerator produces a zero. Similarly, if one samples well above threshold, the regenerator produces a one. However, sampling within the region near threshold, the regenerator output is some percentage of full output. This is undesireable as these signals upon deterioration due to transmission down a long line may be received as a one or zero. In other words there is an uncertainty as to the real identity of the original transmitted signal. One would like to characterize this behaviour of the regenerator which means that one would really like to understand the sampling mechanism of the LD-4 regenerator. Involved in the sampling mechanism are such things as the effect the sampling pulse width has on the regenerating process as well as where does one position the sampling pulse within the incoming signal to ensure an optimum error rate. Sampling pulse width and

* The threshold voltage is a reference voltage which is compared with the heighth of the incoming deteriorated signal. Incoming signals above this level are determined to be ones.

position is important from a design and economic point of view.

Because of the experimental difficulty in determining the position of the sampling pulse with respect to the leading edge of the signal within a few picoseconds, a model for what determines threshold was ignored. Instead an experiment was designed to determine the switching characteristics of the regenerator above threshold, particularly in the transfer region of 10% and 90% full output. In the report to follow, several models were tested for their ability to predict this behaviour. It was hoped that these experiments could have been reproduced using various sampling pulse widths but the regenerator carrier bonds deteriorated.

The experimental results led to several valuable assumptions concerning the regenerator's response. They are as follows:

The uncertainty or transfer region's width is a function of the slope of the input signal.

The smallest uncertainty region can be obtained experimentally without using an idealized square pulse.

The regenerator exhibits hysterisis. The turnoff region is larger than the turnon region.

The sampling pulse should be centred between the two uncertainty regions associated with an incoming pulse. These regions are the turnon and turnoff regions of the regenerator.* However because these two regions are not the same width, the sampling pulse no longer is at the centre of the pulse even though it is centred between

* This concept is clearly illustrated by figure 2.5.5 on page 23 of the report. Further explanation can be found at the bottom of page 22 and the top of page 23.

the two uncertainty regions. This assumption was tested in a mock set-up of the LD-4 system. It was found that the optimum error rate was indeed obtained when the sampling pulse was offset towards the shorter uncertainty region.

The experimental procedure allows one to see clearly how other parameters affect the sampling process by observing how these parameters vary the uncertainty region's width. This method was to be used to find out what effect the sampling pulse width has on sampling but as explained previously, the regenerator's carrier bonds deteriorated.

Experimental results could also be used to explain why the use of a comparator curcuit before sampling and regenerating a pulse circuits helps to improve the error rate. The comparator circuit basically reshapes the deteriorated incoming signal. The reshaped pulse in general has steeper slopes than the original pulse and experimental results show that steeper slopes give rise to smaller uncertainty regions.

ABSTRACT

The switching mechanism of the LD-4 regenerator is studied by applying triangular signals with variable slope and phasing with respect to the sampling pulse in order to investigate their effect on the output signal voltage. Experimental results are obtained in the form of finite sampling crosshairs. These represent the family of input signals that produce all output between the 0 and 1 state. In effect they characterize PST input signals at the N^{th} regenerator to the eventual PST signals at the $N+1^{th}$ regenerator input.

An attempt is also made to correlate the experimental data with either a constant voltage or constant charge sensitivity model in order to understand the mechanism of sampling.

ACKNOWLEDGEMENTS

The author wishes to express his gratitude to Dr. W.F. McGee and the entire staff of department 1E90 for their help and encouragement throughout this project. Dr. McGee's suggestions for project objectives and his guidance were of invaluable aid in undertaking and completing this assignment in the time allotted. Special thanks to Mr. B. Bryden who sacrified much of his own time in order to work very closely with me throughout the project. Mr. Bryden was also of invaluable aid in interpreting the results and in the eventual writing of this report. I would also like to extend special thanks to Dr. M. Frame who gave freely of his time and knowledge in order to increase my understanding of the circuits involved in the LD-4 regenerator. Dr. Frame was also extremely helpful in the writing of this report.

TABLE OF CONTENTS

LIST OF TABLES

LIST OF FIGURES

LIST OF FIGURES (CONT'D)

1. INTRODUCTION

The LD-4 regenerator forms the basis of a long haul digital line operating at a bit rate of 280 Mbits per sec. Figure 1.1 is a block diagram of the repeater. An emitter coupled pair AND gate samples the received, deteriorated PST signal and the regenerator produces an undistorted one or zero for further transmission. Although the aim of the project was to understand the regenerator response, attempts to analyse the response were made in terms of an AND gate model.

There are three aspects concerning the gate's operation:

(i) The effect of sampling pulse width on the gate output.

(ii) Positioning of the sampling pulse for maximum sensitivity.

(iii) Establishing a threshold level above which incoming signals are determined to be 1's.

This project is concerned only with the last two aspects of the gate's operation. The idea of a sampling crosshair embodies both of these aspects by representing the threshold with a horizontal line and the sampling pulse position with a vertical line. This is shown in Figure 1.2.

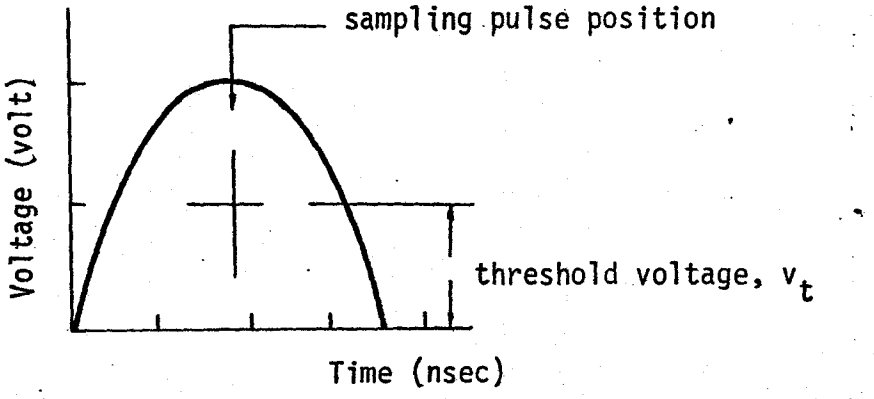

Fig. 1.2 Diagram illustrating the input PST signal with the ideal crosshairs superimposed.

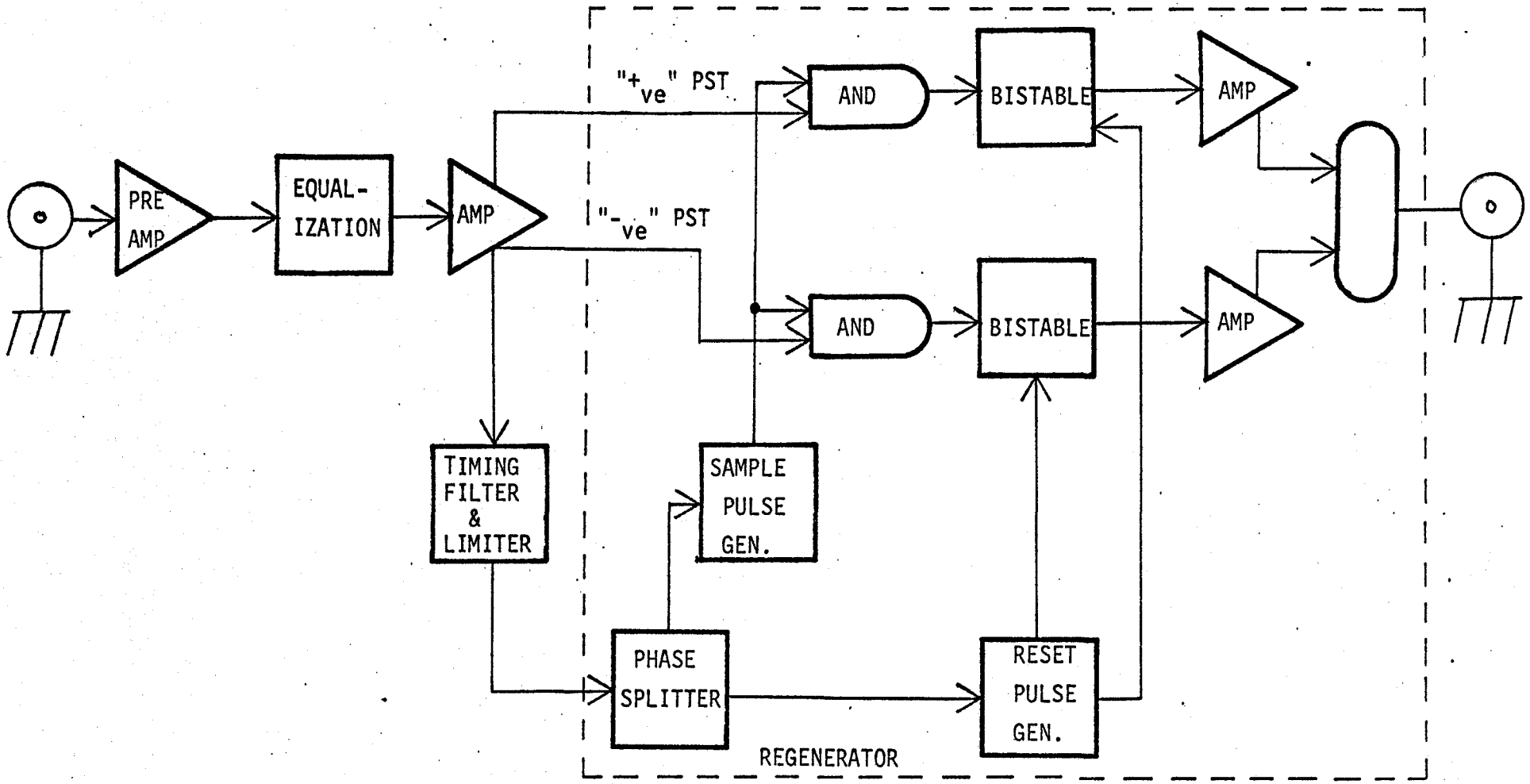
PRE AMP
EQUAL-IZATION
AMP
"+ve" PST
"-ve" PST
AND
AND
BISTABLE
BISTABLE
AMP
AMP
TIMING FILTER & LIMITER
SAMPLE PULSE GEN.
PHASE SPLITTER
RESET PULSE GEN.
REGENERATOR

The combination of AND gate and bistable does not switch instantaneously from the low state zero to the high state one. There are uncertainty regions about the threshold and the sampling pulse position as shown in Figure 1.3.

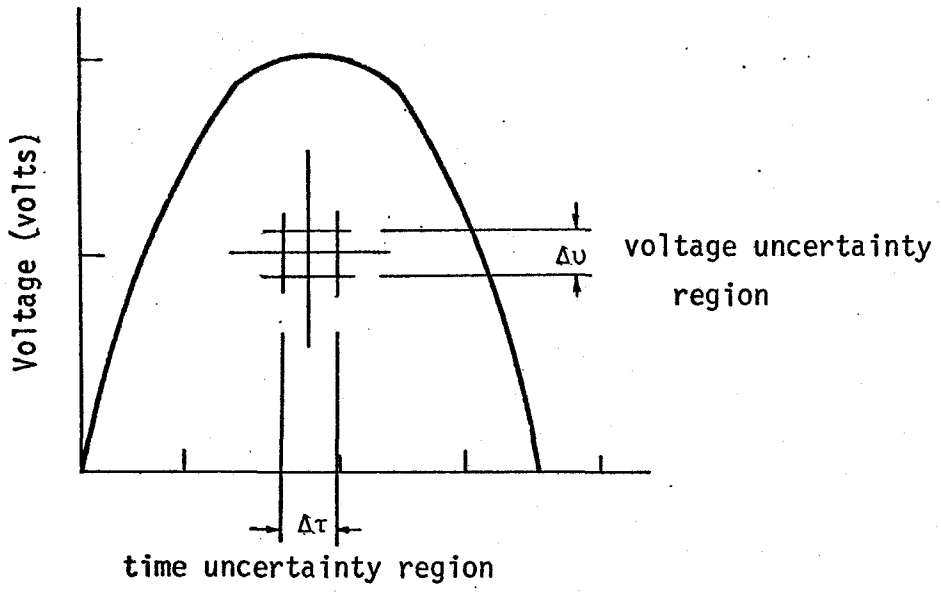

Fig. 1.3 The PST input curve with the finite sampling crosshairs superimposed. The size of the crosshairs are exaggerated. $\Delta\tau$ is typically 10 picoseconds and Δv is typically 50 millivolts.

An input signal with an amplitude lying within the voltage uncertainty region shown in Figure 1.3, may be horizontally displaced in time up to a distance of $\frac{\Delta\tau}{2}$ picoseconds in either direction about the centre line and the bistable - AND gate combination will produce output between the states "one" and "zero". It is this finite heighth and width of crosshair that the experiment investigated. Two models are assumed for regenerator operation in the transition region: a constant voltage sensitivity model and a constant charge sensitivity model. By comparing the experimental

crosshairs with those predicted by the two models an understanding of the regenerator's operation can be obtained.

2. EXPERIMENT

2.1 Input Signals

This section is intended to supply sufficient background for the development of the experiment.

The input to the regenerator is a bipolar PST signal which can be used to construct an eye diagram by superimposing all possible sequences of 1's, 0's and -1's. This is illustrated in Figure 2.1.1. The eye diagram is useful for defining the three main aspects of the gate's operation; sampling pulse width, sampling pulse position, and the threshold level. (1)

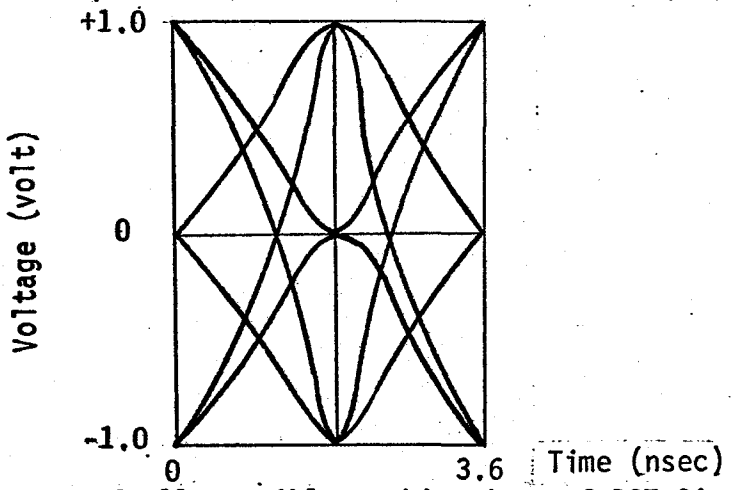

Fig. 2.1.1 Eye Diagram of all possible combinations of PST Signals

In the experiment an approximation to the shape of the crosshairs was obtained by obtaining the marginal eye opening for 10% and 90% output which approximates the limits of the transition region of the regenerator's transfer function. The actual position of the crosshair within the eye can not be determined. The position of the sampling pulse with respect to the input signal

can't be measured accurately at the AND gate's input because of the poor terminating impedance. Input impedance to an emitter coupled pair AND gate varies during switching between 2K and infinity (2). Figure 2.1.2 shows the gate. In order to increase the return loss, a 10 pf. capacitor was placed at the input. However, this capacitor had the undesirable effect of rounding the input signal, preventing any accurate determination of the sampling pulse's position as illustrated in Figure 2.1.3. Therefore the trade-off in the capacitor's size resulted in a return loss for the gate of 12 dB at 200 MHz instead of the desired 26 dB.

Experimentally, the actual PST signals are characterized by a family of triangular curves with variable slopes. These triangles are used to approximately construct the finite crosshairs by superimposing an input triangle in the four positions required

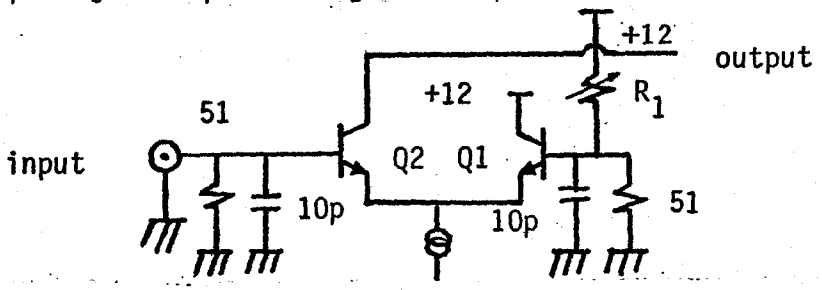

Fig. 2.1.2 AND Gate

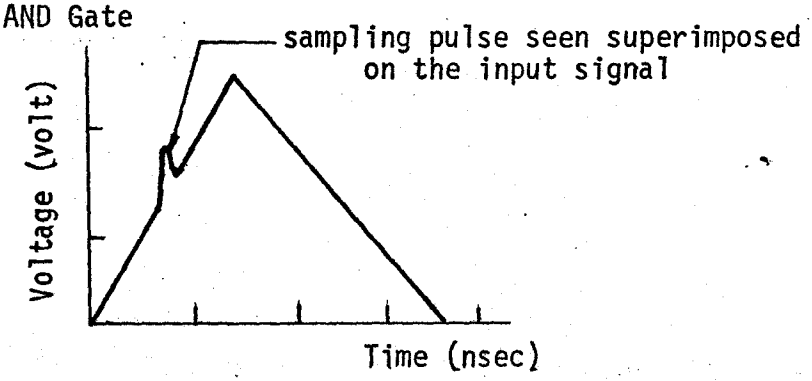

Fig. 2,1.3 Input Signal at the AND Gate showing the notch due to the sampling pulse.

to give 10% and 90% output, i.e. the turn-on and turn-off regions of the regenerator. This construction is illustrated in Figure 2.1.4.

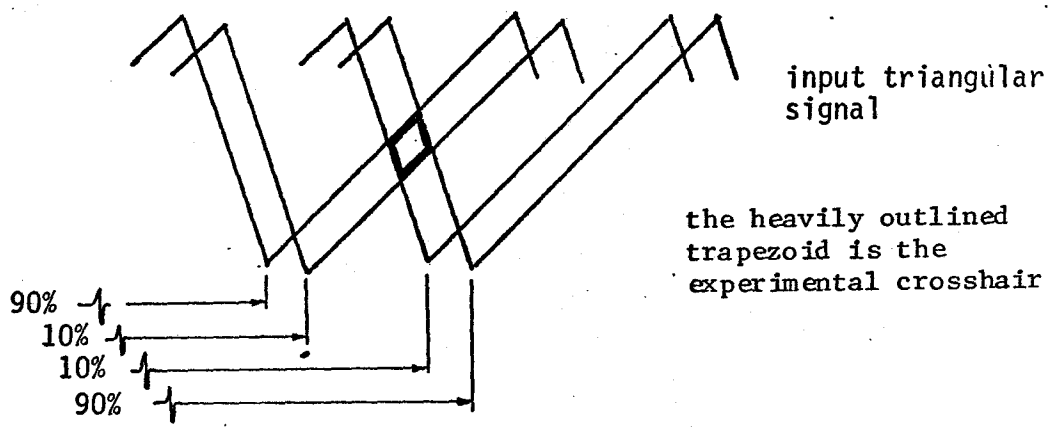

Fig. 2.1.4 Construction of the Crosshair

2.2 Constant Voltage Sensitivity Model for Triggering the Regenerator

In this model the output voltage of the regenerator depends only upon the voltage at the input of the regenerator. The regenerator compares the input signal with a reference threshold. For input signals above this threshold the regenerator output tends towards full output as the input signal tends towards one. This output is proportional to the input voltage within the uncertainty region.

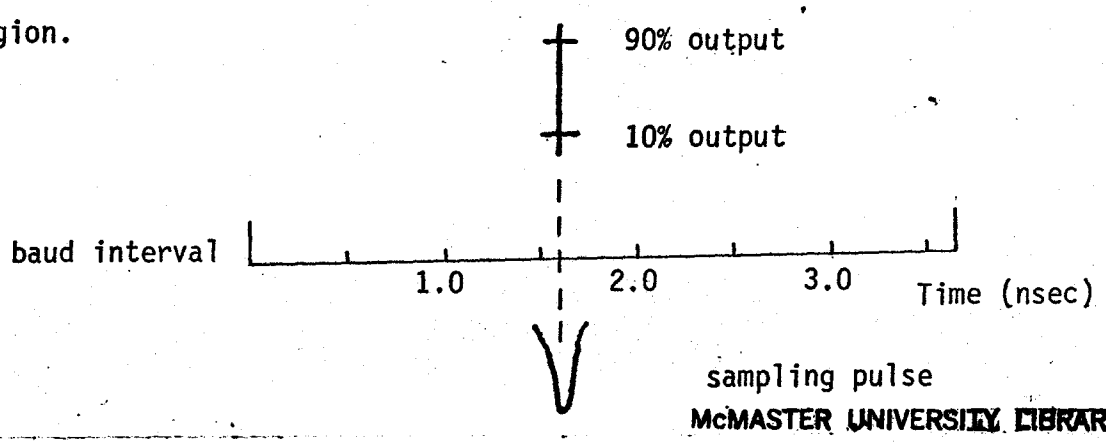

Fig. 2.2.1 Regenerator crosshair illustrating the 10% and 90% output levels.

The regenerator can be considered to have a crosshair of the type illustrated in Fig. 2.2.1. The crosshair's location in the baud interval is fixed according to where the sampling pulse is positioned. The levels 10% and 90% of maximum output voltage are arbitrarily chosen to represent the regenerator starting to produce output and the regenerator reaching its maximum output. The input voltages corresponding to these two outputs are represented by the two horizontal lines which are separated by the constant amount designated as Δv.

If an input triangular signal is shifted with respect to this crosshair, i.e. the sampling pulse, there will be points on the input signal corresponding to 10% and 90% voltage output levels of the regenerator. A diagram superimposing the input signal in the four positions which resulted from shifting the triangular input signal with respect to the sampling pulse to give 90%, 10% then 10%, 90% output is shown in Figure 2.1.2. The resulting trapezoid encloses the crosshair that the regenerator has associated with its sampling mechanism as previously mentioned in section 2.1.

Note that the crosshair for a voltage dependent regenerator is symmetrical about the vertical line representing the constant test position determined by the sampling pulse position. This is true only in the absense of hysterisis which has been assumed in deriving this model.

A regenerator which is not described by this model can be expected to produce asymmetrical crosshairs similar to the one illustrated in Figure 2.2.2.

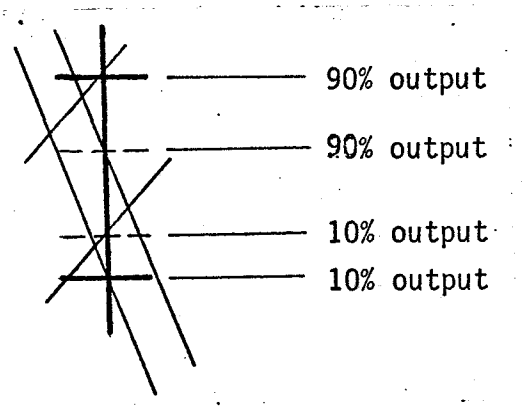

Fig. 2.2.2 Asymmetrical crosshair showing the 90% and 10% levels changing for each input. The sampling position is constant.

Note that the 90% and 10% input test levels are not constant for a particular sampling test position which contradicts the constant voltage sensitivity model above. Figure 2.2.2 can also be interpreted as a shifting sampling position as shown in Figure 2.2.3. This interpretation also contradicts our particular model which assumes a constant sampling pulse test position independent of the input signal.*

* Such a model can be realized with a transistor that switches whenever the reverse bias at the base is exceeded by the input signal. If the reverse bias changes due to temperature instability then the threshold reference level also changes. More detail on circuit analysis of the constant voltage sensitivity model is given in Appendix A.

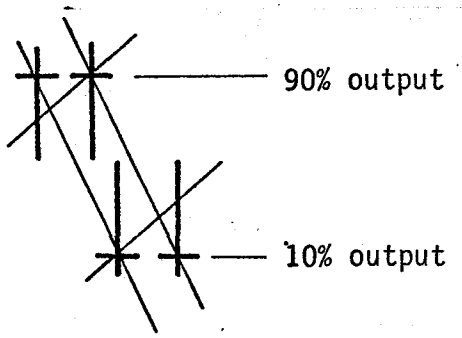

Fig. 2.2.3 Asymmetrical crosshairs. The sampling pulse test position changes with each input signal. For clarity only the relevant part of each crosshair is shown.

A mathematical description for a constant voltage sensitivity model can be derived from the crosshairs as shown in Figure 2.2.4. Using the rising edge of the triangle, the slope S is equal to

$$S = \Delta v/\Delta\tau \qquad |1|$$

where Δv is the voltage difference between 10% and 90% output and $\Delta\tau$ is the time difference between 10% and 90% output. Since Δv is assumed constant then

$$S \propto \Delta\tau^{-1} \qquad |2|$$

The relationship for the falling edge of the triangle is the same.

If the condition of constant sampling pulse test position were relaxed, equation |2| still holds, but the proportionality

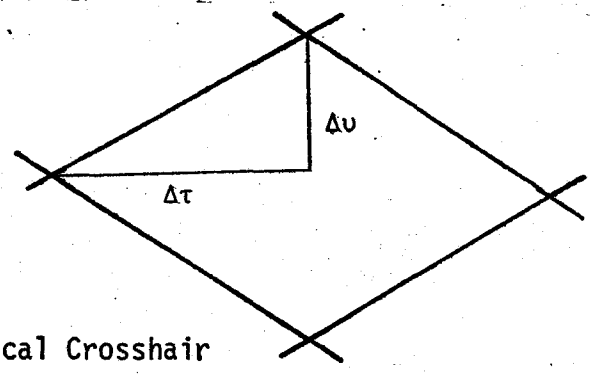

Fig. 2.2.4 Symmetrical Crosshair

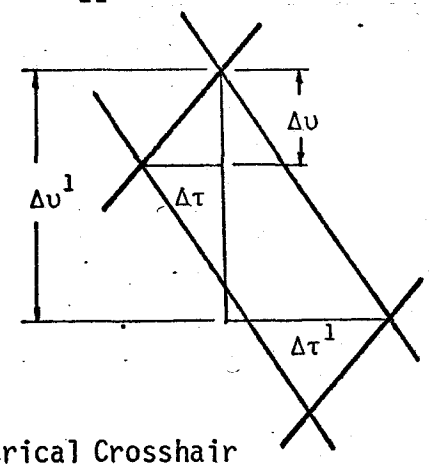

Fig. 2.2.5 Asymmetrical Crosshair

constant Δv^1 for the falling edge is different than Δv for the rising edge. This is illustrated in Figure 2.2.5. A circuit operating in this manner can be assumed to have hysterises associated with it. If the crosshairs were drawn using the same slope for the rising and falling edge but different Δv's then the hysterisis becomes readily apparent. See Figure 2.2.6.

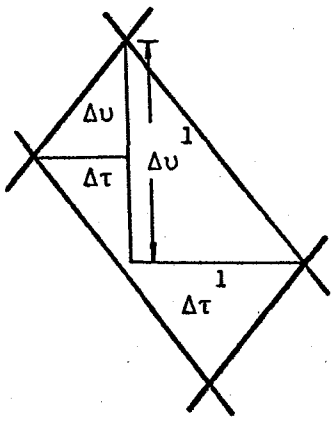

Fig. 2.2.6 Crosshair construction using equal slopes for the rising and falling edges of the input signal. The hysterisis now becomes readily apparent showing $\Delta\tau^1$ to be greater than $\Delta\tau$.

2.3 Constant Charge Sensitivity Model for Controlling the Regenerator Output

The model presented here postulates a constant charge sensitivity to inputs above a defined voltage referred to as the threshold voltage. The threshold voltage required for regenerator output to occur is determined by a particular voltage and does not change when inputs other than the defining DC level enter the AND gate. Therefore the threshold can be represented by a DC level and only a constant charge above this level will be considered responsible for increasing output from 10% to 90% maximum value.

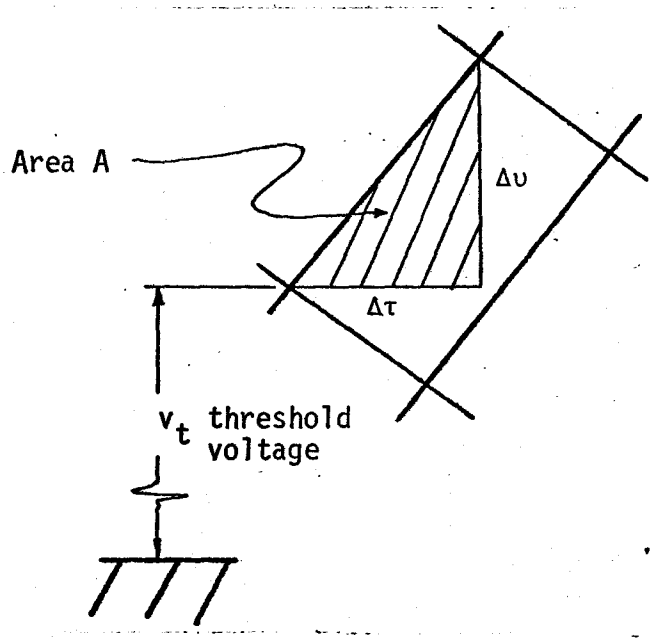

Fig. 2.3.1 Model of input signal for constant charge model.

From Figure 2.3.1 the equation for the slope is

$$S = \Delta v/\Delta\tau \qquad |1|$$

Area A of the input signal above threshold level is

$$A = \Delta v\Delta\tau/2 \qquad |3|$$

$$A = S\Delta\tau^2/2 \qquad |4|$$

With the assumption of constant area eqn. |4| becomes

$$S = \frac{2A}{\Delta\tau^2} \qquad |5|$$

A graph of S vs. $\Delta\tau$ on log-log paper will give a straight line with a slope of -2. Note that the threshold voltage does not enter the calculations.

The amount of charge absorbed can be calculated from the log-log graph. Equation |5| on log-log paper becomes

$$\log S = \log 2A - 2\log\Delta\tau \qquad |6|$$

If $\Delta\tau$ is set equal to 1 then

$$\log S = \log 2A \qquad |7|$$

On log-log paper, 2A can be read directly at $\Delta\tau = 1$, Area A can be related to charge quite simply from equation |4|. Equation |8| gives the dimensions of A.

$$A = \frac{\text{volts}}{\text{nsec.}} \times (\text{psec})^2 \qquad |8|$$

If A is divided by input impedance, equation |8| becomes

$$A = \frac{\text{volts}}{\text{ohms}} \times (\text{psec}) \times 10^3 = \text{amps} \times \text{psec}$$

$$= \text{picocoulombs} \qquad |9|$$

2.4 Experimental Results

The experimental set up is shown in Figure 2.4.1.

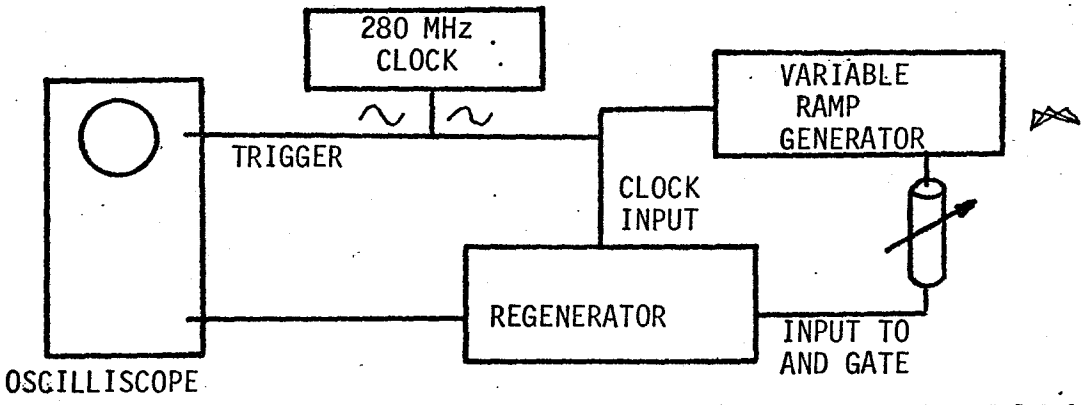

Fig. 2.4.1 Block Diagram of the Experimental Set Up.

A variable ramp generator was constructed to provide triangles of variable slope with the same heighth and period but no DC offset. These triangular inputs were sampled at various points by shifting the input signal rather than the sampling pulse. A relative delay between the short pulse and the input signal was introduced using the variable air line in the input signal cable. The position of the air line that gave 90% output was noted and more delay was added until the output reached 10% maximum output. The resulting phase shift $\Delta\tau$ between the 2 outputs was recorded. Again, more delay was added until the 10% output point on the falling edge of the triangle entered the AND gate. This position was noted and additional delay added until the output reached 90%. The phase shift for the falling edge was also recorded.

The effect of shifting the input signal can be seen more clearly as a relative shifting of the sampling pulse as illustrated in Figure 2.4.2.

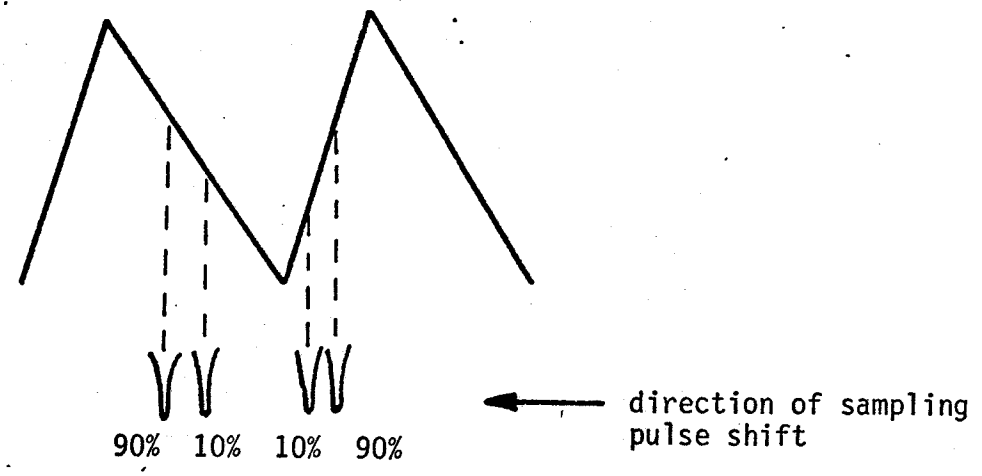

Fig. 2.4.2 Shifting the input signal with respect to the sampling pulse is the same as shifting the sampling pulse with respect to the input signal.

Attempts to obtain photographs of an undistorted input signal at the input of the AND gate were impossible due to the gate's poor input termination.* In order to obtain a superimposed picture of the input signal in the four positions mentioned previously, the input to the regenerator and gate was removed and applied to the 50 ohm termination of the oscilliscope where the four input signal phase positions were reset and photographed.

The crosshairs obtained from these photographs were asymmetrical as shown in Figure 2.4.3. The photographs suggest that either the circuit does not follow a constant input voltage sensitivity model since a constant sampling position can't be

* Already discussed in Section 2.1.

defined, or the circuit has hysterisis.**

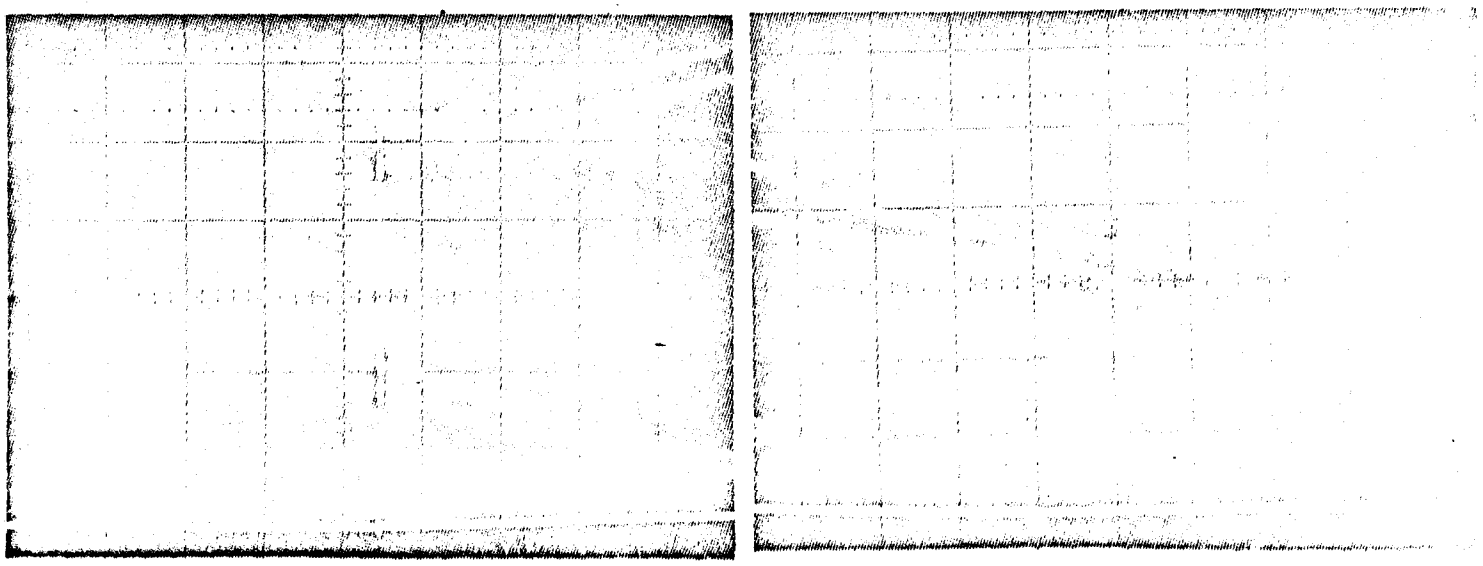

Fig. 2.4.3 Photographs showing assymetrical crosshairs.

The slopes S of the rising edge of the input triangles were plotted against $\Delta\tau$, the phase shift required to shift the output from 90% to 10% of the maximum value. Also graphed are the slopes S of the triangles' falling edges against $\Delta\tau$ the phase shift between 10% and 90% output. Figure 2.4.4 shows the 2 curves as well as other points obtained during a repeat of the experiment some time later.*** Both S vs $\Delta\tau$ curves as well as

** Justification for this statement given in section 2.2.

*** Further measurements were impossible as the wire bonds in the AND gate carrier began to deteriorate, increasing the time between the 10% and 90% output levels. Figure 2.4.5 is a photograph of the wire bonds. This phenomena began appearing throughout the circuit and switching times in excess of 400 picoseconds were recorded.

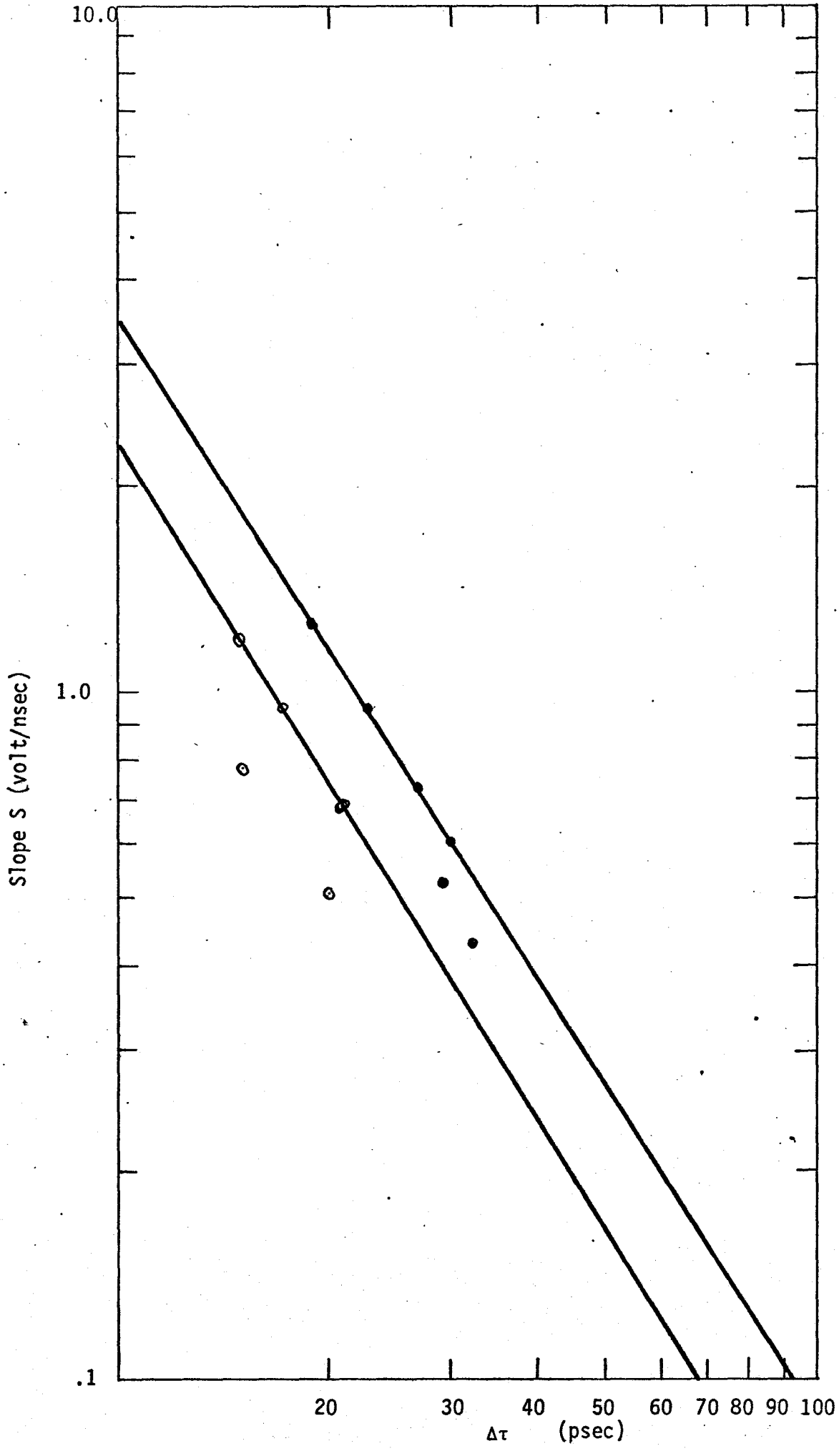
10.0
1.0
.1
Slope S (volt/nsec)
20
30
40
50
60
70
80
90
100
Δτ (psec)

the extra points were graphed on log-log paper to test for a power relationship.

Equation |10| is the resulting relationship obtained from the log-log graph for the rising slope. Equation |11| is the S vs $\Delta\tau$ relationship for the falling slope of the input triangle. The two curves are separated by a phase shift as illustrated in Figure 2.4.4.

$$S_r = 98\Delta\tau^{-1.63} \qquad |10|$$

$$S_f = 157\Delta\tau^{-1.63} \qquad |11|$$

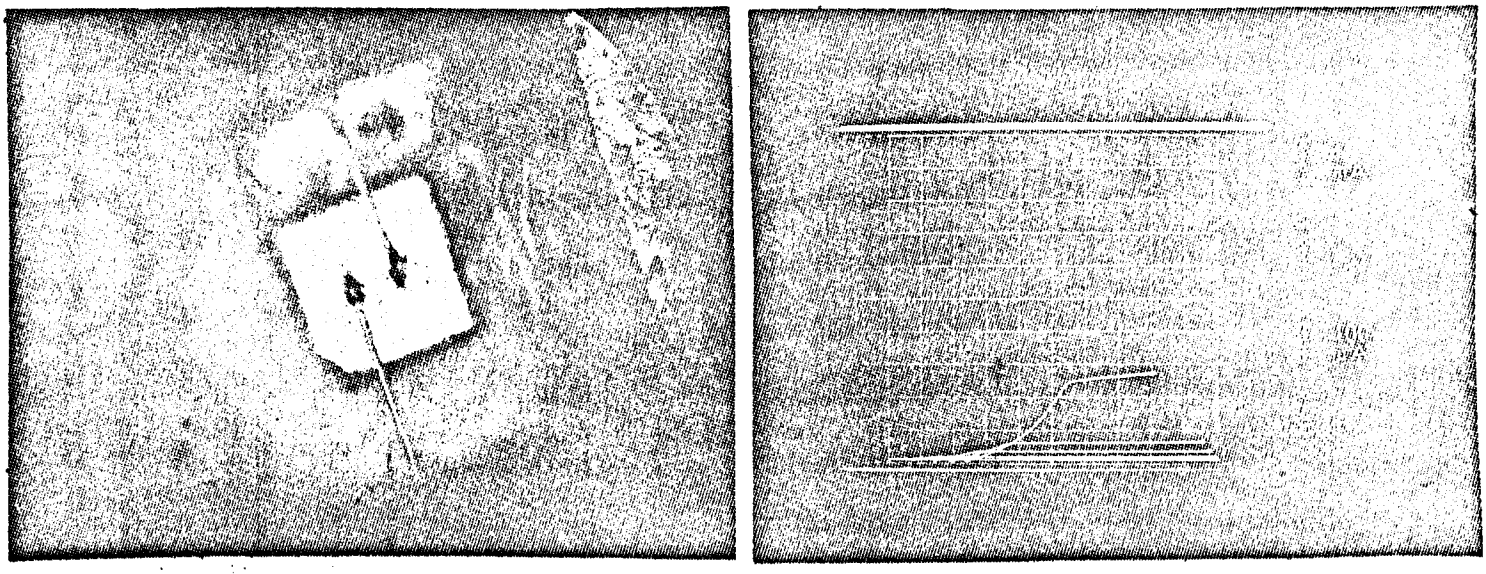

Fig. 2.4.5 The deteriorated wire bonds are illustrated on the left. The photograph on the right is the resulting characteristic of the carrier.

2.5 Discussion

The experimental exponent of $\Delta\tau$ in the S vs $\Delta\tau$ relationship is -1.63 which is between the exponents required for the constant

voltage and constant charge sensitivity models. Experimentally, the assumption of a constant threshold was partially demonstrated but not conclusively since the actual threshold may be displaced from the crosshairs.

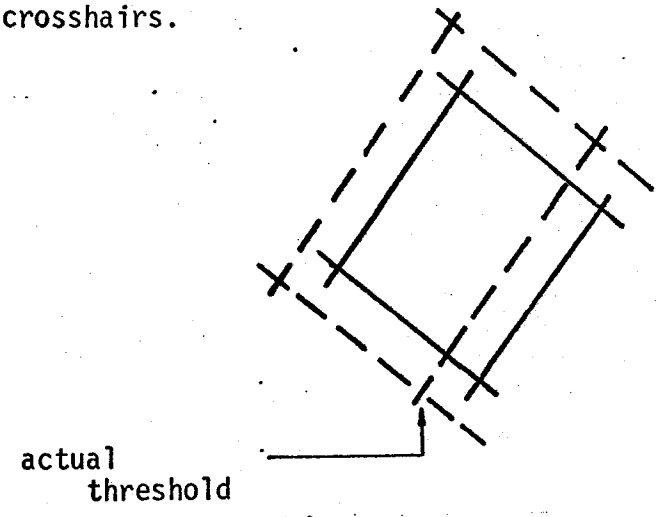

Fig. 2.5.1 The solid line crosshair is the one seen at the AND gate's input by the experimenter. The effective crosshair is the dotted line and results from a constant delay between the input signal and output response.

The threshold level was assumed to be the bottom of the crosshairs, i.e. where the two slopes giving 10% output crossed. Table (2.5.1) lists the threshold levels so defined.

In Figure 2.5.2 the S vs $\Delta\tau$ graph of the constant voltage model and the S vs $\Delta\tau$ graph of the constant charge model is compared with the experimental s vs $\Delta\tau$ graph for the falling edge of the input triangle. By examining the constant voltage and constant charge models, the behaviour of the S vs $\Delta\tau$ graph can be postulated for the limits of S approaching zero and infinity.

RISING SLOPE (tan)	FALLING SLOPE (tan)	Δv (volts)
..530	1.02	5.6
.695	.728	5.6
.965	.952	5.6
.304	1.27	5.6
.436	.98	5.4

Table 2.5.1 Threshold Voltages

In the limit as S approaches infinity, $\Delta\tau$ becomes finite since it is physically impossible to have a zero phase shift between 10% and 90% maximum output. The high frequency components associated with steep slopes suggests that the circuit favours a constant charge model.* Figure 2.5.2 also illustrates how the steeply varying constant charge curve resembles a curve having a finite $\Delta\tau$. The finite $\Delta\tau$ is the time uncertainty width associated with the finite crosshairs and defined by applying a unit step and varying the phse of the edge with respect to the sampling pulse position. If a curve were fitted to experimental results containing more points, an estimate of the time uncertainty width could be made.

* See Appendix A

The graphs of the constant voltage and constant charge models were produced by taking one of the experimental points and using its coordinates to calculate other points. For the constant voltage and charge graphs, Δv and A respectively were kept constant while the slope was varied and the resulting $\Delta\tau$ calculated.

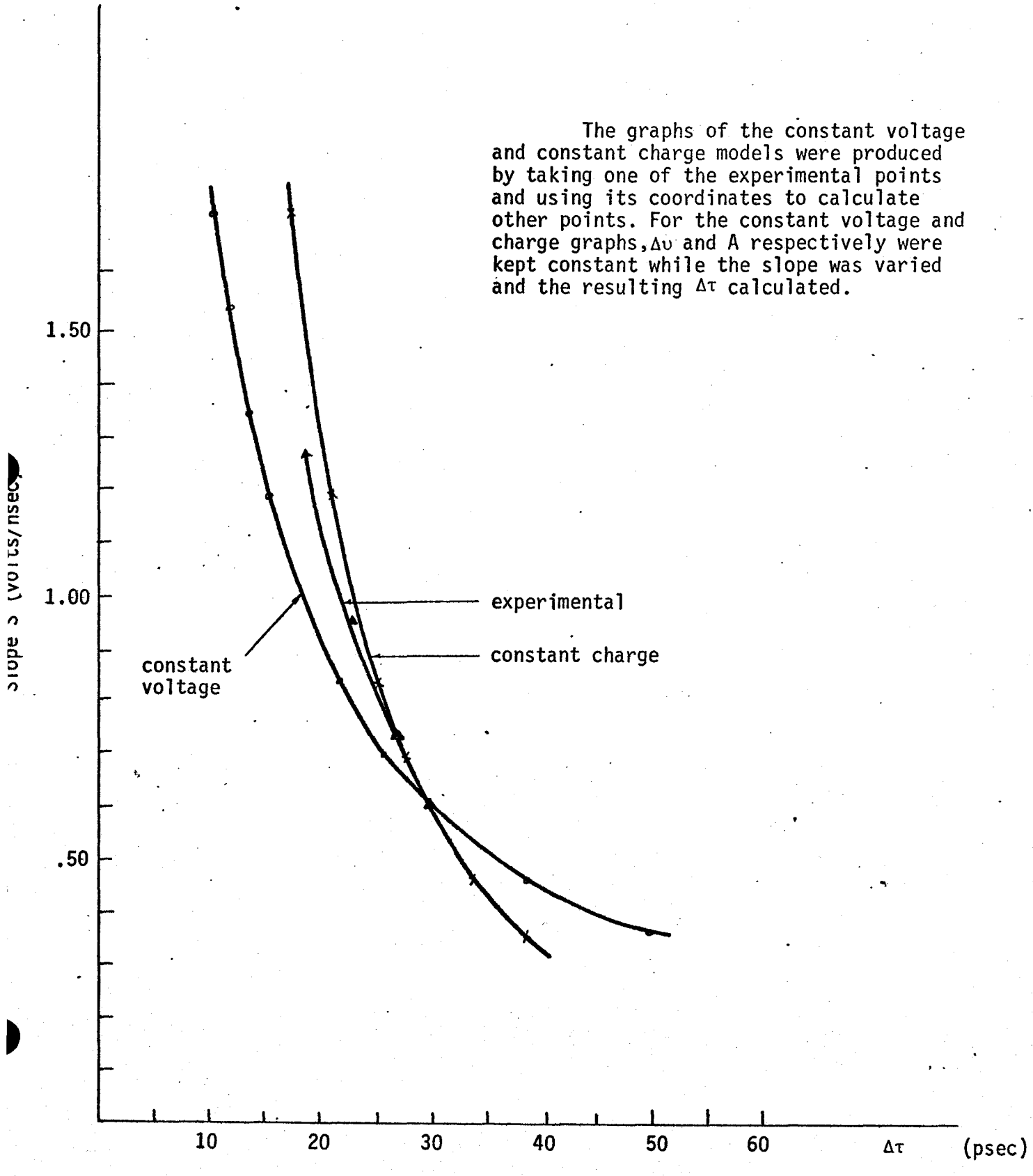

In the limit as S approaches zero ie. a DC signal, $\Delta\tau$ approaches infinity but Δv the input voltage difference corresponding to the output voltage change between 10% and 90% output, remains finite. The experimental S vs. $\Delta\tau$ curve becomes a constant voltage relationship as S approaches zero. Figure 2.5.3 illustrates the experimental curve with its postulated limits.

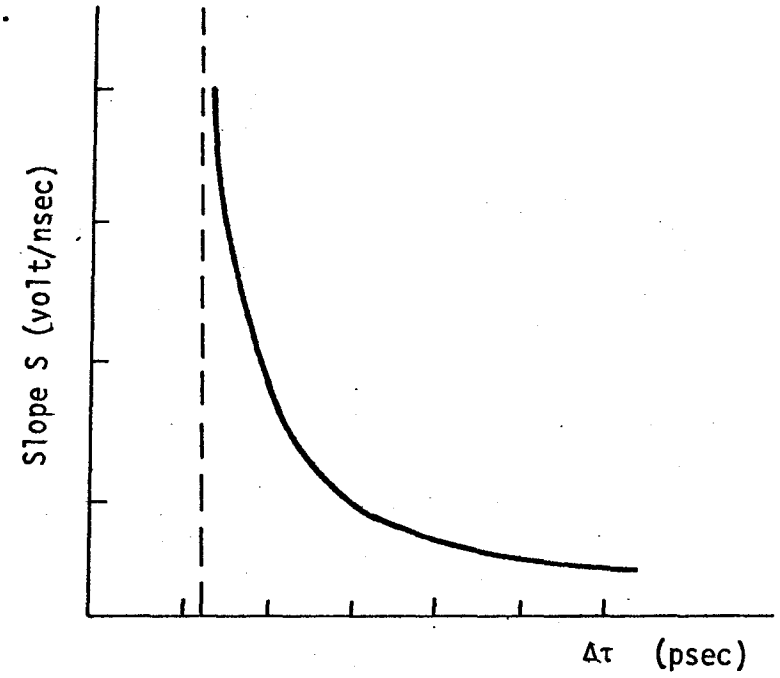

Fig. 2.5.3 The experimental S vs $\Delta\tau$ curve with postulated limits.

The relative widths of the uncertainty regions of the crosshairs also affect the optimum position of the sampling pulse. Figure 2.5.4 illustrates the input signal with the uncertainty regions superimposed. To the regenerator, the input signal resembles the multi-regional box illustrated in Figure (2.5.4).

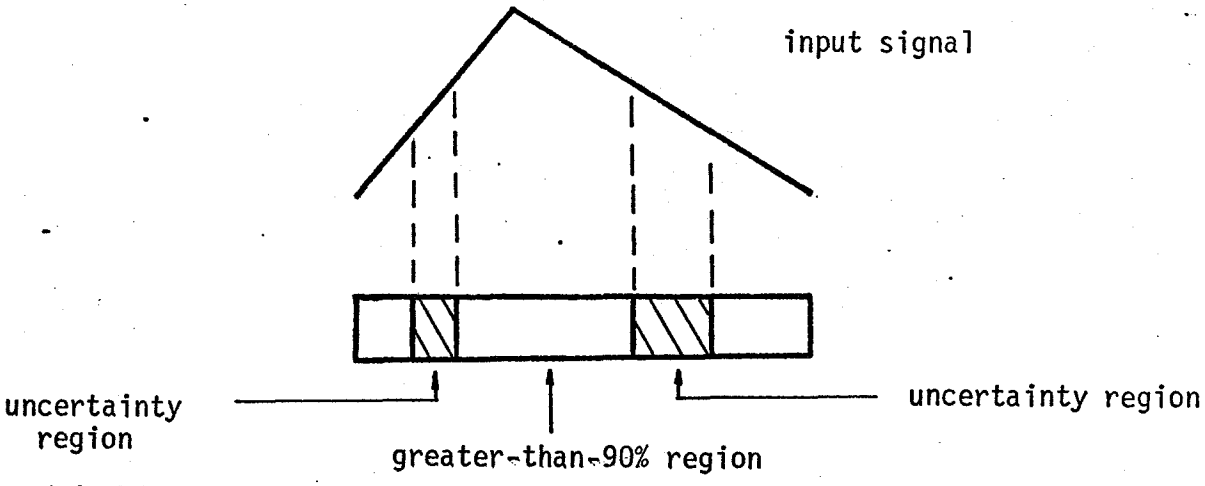

Fig. 2.5.4 Representing the input signal as a multi-regional box. The sampling pulse must be positioned within the greater than 90% output region in order to ensure regenerator output larger than 90% maximum output. This is illustrated in Figure (2.5.5).

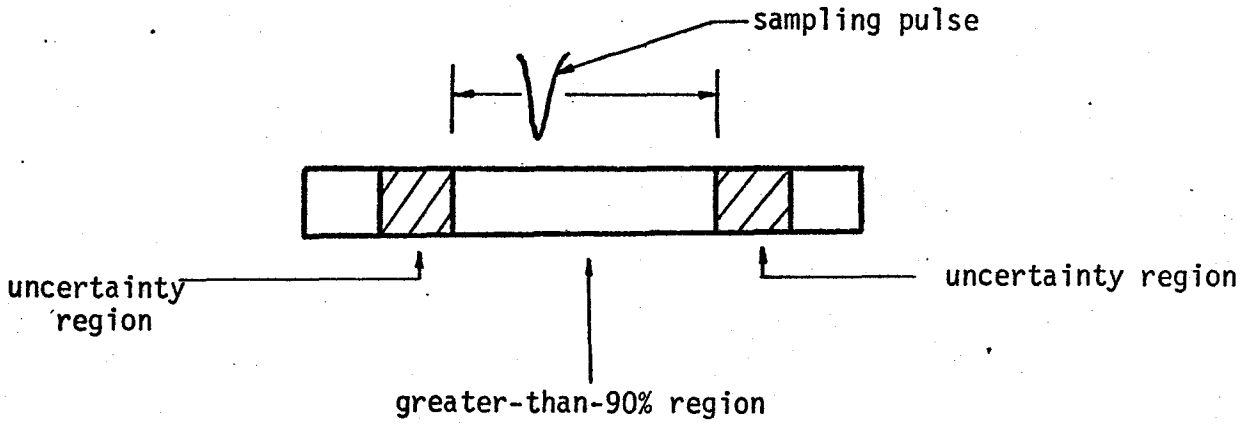

Fig. 2.5.5 The sampling concept using the multi-regional box of Figure 2.5.4.

If the sampling pulse were to fall within the uncertainty region, the output could not be predicted. It is the output uncertainty within this region that leads to errors.

The S vs. $\Delta\tau$ graphs in Figure 2.5.2 for the rising falling edges of the input triangle reveal the circuits hysterisis. The turn off region corresponding to the falling edge has larger $\Delta\tau$'s than the turn on region for the rising edge. Partial explanation for this hysterisis can be obtained from the different behaviour that the input capacitance and impedance exhibit when a rising and falling edge are applied to the input.* If both uncertainty regions were equal then the sampling pulse would be positioned in the centre of the input signal. Since the turn off uncertainty region is larger than the turn-on region, the sampling pulse's optimum position is offset to the left towards the turn on transition region.

2.6 Conclusions

The regenerator operation is more complicated than the constant voltage or constant charge sensitivity models suggested. Both models, including expected deviations were suggested by a hybrid π model of the AND gate transistors.**

* The input impedance decreases with an applied rising edge and increases towards infinity for an applied falling edge. The reverse is true for the input capacitance. The result is that the circuit charges more quickly for a rising edge than for a falling edge (3).

** Appendix A gives some justification for the constant voltage and charge models assumed.

However, in order to accurately describe this high frequency circuit a non-linear model must be used. The regenerator's switching mechanism to a first order approximation can be described by the hybrid π model. This suggests that a sufficiently accurate model of the AND gate modified to account for phenomena introduced by other circuits in the regenerator can be used to accurately represent the regenerator during switching.

The analysis of an experimental S vs $\Delta\tau$ graph with sufficient point allows the calculation of the time uncertainty of the repeater. This result would be impossible to obtain by other means.

The hysterisis associated with the uncertainty regions explains the need for offsetting the sampling pulse from the centre of the eye.

Repetition of the experiment produced points not on the straight lines of equation (10) and (11). Error bars of ± 1 picosecond are sufficient to describe the measurement errors arising from the calibration of the delay line and measuring 10% and 90% output from the regenerator. Discrepancies of 2 picoseconds or greater suggest that the measurement technique is not to be faulted for the errors. Such errors result from the changing of the regenerator's characteristics. The regenerator was very sensitive to external noise and temperature variations since there was no temperature stability compensation included.

Further experimentation was terminated due to the deterioration of the wire bonds for several carriers used in the regenerator.

3. REFERENCES

(1) F.D. McAllum, "Description and Specifications for Phase I of the 280 Mbits per second Digital Repeatered Line", Dept. 1E90, Aug. 1969.

(2) C.S. Meyer, D.K. Lynn, D.J. Hamilton, "Analysis and Design of Integrated Circuits", New York: McGraw-Hill, 1968, p. 171.

(3) B. Bryden, Patent Application, "High Speed Pulse Generator", Sept. 1971.

(4) C.S. Meyer, D.K. Lynn, D.J. Hamilton, "Analysis and Design of Integrated Circuits", New York: McGraw-Hill, 1968, p. 37.

APPENDIX A

DERIVING CONSTANT VOLTAGE & CONSTANT CHARGE MODELS FROM TRANSISTOR MODEL

The constant voltage and constant charge models described in this report can be derived from the hybrid π model of the AND gate transistors illustrated in Figure A.1.*

At high frequencies the impedance of Cd is much less than rbb' and the circuit roughly approximates a simple integrator with the capacitor on a voltage pedestal equal to V_{ref} -.8 volts above ground. Any input signal above this pedestal is integrated by the combination of Cd and rbb'.

At low frequencies the capacitor Cd is effectively shunted by the resistor re, making the input impedance basically a resistive voltage divider. The input current is not simply related to V_{in} by the constant $\frac{1}{R_{in}}$ since R_{in} is current dependent. Since the output current I_C is equal to $\beta \times I_b$ the transistor itself is a current sensitive device. However, by putting the small load resistor R_L in parallel with the large input impedance of the transistor, the input impedance of the circuit becomes fairly constant and independent of current. This makes the circuit more voltage dependent.

* A charge model would give more physical insight into the operation of the circuit. However, the degree of approximation for both models is the same (4) and a more accurate circuit description can not be obtained without a non-linear model. The hybrid π was used because of its simplicity and its familiarity to the reader.

822 c

"LASING ACTION" IN HIGH THRESHOLD ELECTRON BEAM PUMPED CdS PLATELETS

by

Stephen J.G. Brown

"PART B:" MCMASTER ON-CAMPUS PROJECT*

A project report submitted in partial fulfillment of the requirements for the degree of

Master of Engineering

Dept. of Engineering Physics

McMaster University

Hamilton, Ontario

May, 1973

* One of two project reports: The other part is designated PART A: INDUSTRIAL PROJECT

ACKNOWLEGEMENT

I am deeply indebted to Dr. Garside for his guidance on this project.

ABSTRACT

Results of a detailed investigation of the time-dependence of the stimulated emission from electron-beam pumped CdS platelets are reported. Unlike lower threshold platelets previously reported (1), the platelet examined here exhibits rapid tuning with time of the stimulated emission to longer wavelength. The rate of this frequency tuning compares favourably with the value reported by Shewchun et al (2) for CdS crystals many times thicker and with a higher threshold than the one measured in this report. Furthermore, there is a temporal variation of the angular position of the spatial mode. This temporal variation or angular tuning rate was compared with angular tuning data reported for GaAs and CdSe as well as with the theory that predicts such tuning in these crystals (3).

LIST OF FIGURES

INTRODUCTION

The presence of stimulated emission in the output from electron beam-pumped Cds bulk crystals was reported by Shewchun (2) in 1970. However, few details were given concerning the rapid tuning of stimulated emission towards longer wavelength with increasing time from the start of the pumping pulse. Furthermore, no attempt was made to examine the deviation of the far field radiation pattern of the spatial laser mode with respect to the cavity axis and the changes of this angle during the excitation pulse. Effects of the first type were termed frequency tuning and the effects of the second type were termed angular tuning. Both angular and frequency tuning were examined here in detail for a platelet with a lasing threshold considerably higher than those previously reported by other authors (1). This consideration of a high threshold platelet is important for it has been found that rapid wavelength tuning, which is independent of pumping intensity above threshold, does not occur for relatively lower threshold platelets such as those examined by other authors as well as those examined within this experiment.

The data presented in this paper for the angular variations of the far field laser radiation pattern and its subsequent change during the excitation pulse will be compared with predictions from an analytical model for the electron-beam pumped semiconductor laser system presented by Kawasaki (3). The model predicts that the degree of variation of the laser beam from the cavity axis depends on the size of the index step. The index step is the spatial variation in the index of refraction between the pumped and unpumped region. The spatial mode which gives rise to the far field laser radiation pattern was assumed to be of the form

$$A = \sin(px) \quad \text{in } (0,d) \quad (1)$$

$$A_o \exp(-qx) \quad \text{in } (d,\infty)$$

where p,q are complex, A is the amplitude of the spatial mode, x is the distance from the pumped surface of the crystal, and d is the width of the pumped region. The model predicts that the index step tends to confine the spatial laser mode. The larger the index step, the more confined the spatial mode is within the pumped region d and less angular deviation should result for the far field radiation pattern of the spatial mode.

In order to test the assumption-that it is the increasing confinement of the spatial mode in time due to the index step increasing in time-that creates the tuning of the far field radiation, the spatial mode should be partly confined within the pumping region at the onset of excitation. Complete confinement would give no initial angular deviation and subsequently no angular tuning. Confinement of the spatial mode can be accomplished by creating an extremely large index step within the pumping region depth d at the onset of excitation, or by using a platelet which has a thickness equal to the pumping region depth. The second situation approximately exists for the platelet examined within this paper.

EXPERIMENTAL PROCEDURE

Light emission from the semiconductor samples were produced by means of pulsed electron-beam pumping. The pulsed mode of operation was used in order to reduce heating of the samples to acceptable levels. Pulse length was 220 nsec. at a repetition rate of 60 Hz. A magnetic lens was used to focus and position the beam on samples mounted on the cold finger of a dewar, kept at 77°K. Both sample and electron gun were in the same vacuum chamber. The emitted light was focused either on the entrance slit of a motor driven monochromator fitted with a S-11 photomultiplier tube or directly to the photomultiplier through a single slit. The output of the detector was observed with either a Hewlett-Packard sampling scope, triggered from a portion of the incident beam, or displayed on a strip chart recorder. More details on the experimental setup appear in (2).

The samples were prepared by cleaving two Fabry-Perot faces parallel to the c axis of the CdS platelet. The experimental data presented here was obtained using a crystal 1000 x 150 x 10 microns thick. The 150 microns is the cavity length. The samples were mounted on the copper finger of the dewar with indium solder.

LASING ACTION AND LASER MODES

A number of authors have used various criteria to indicate the presence of lasing action in pulsed semiconductor lasers. Superlinearity of the output light intensity as a function of pumping current, spectral narrowing of the light emission, spatial coherence, a well-defined frequency mode pattern and the abrupt appearance of spatial modes are criteria typically employed. A detailed analysis of the applicability of such criteria is presented in reference (2). It is concluded that a satisfactory operational indication of the onset of lasing action is given by the sudden occurence of sharp Fabry-Perot modes at pumping current densities corresponding to the upper end of the superlinear region of the output intensity curve plotted logarithmically as a function of excitation current.

Figure 1 shows the detected light output, integrated over both wavelength and time as a function of pumping current density for three different electron beam voltages. It is evident from a comparison of the three curves that the current required to produce saturation in the light emission shifts rapidly to higher values as the excitation voltage is reduced. Changes of a similar nature have been observed in GaAs and ZnO lasers (4)(5). The curves in figure 1 illustrate the linear increase of the light output at low pumping levels, a superlinear region indicative of the presence of significant stimulated emission, and a second linear (saturated) region above threshold. Figure 2 shows the spectral nature of the light output, integrated over time, for two beam current densities at a beam voltage of 30 kv. These high visibility mode curves occur for a current of approximately 3.0 A/cm^2 which

corresponds to the upper end of the superlinear region of the 30 kv. curve in figure 1. Thus it may be said that lasing action occurs in this crystal for current densities above 3.0 A/cm^2. This threshold current is higher than that measured for several other crystals of similar dimensions. Threshold currents between 1.0 and 2.0 A/cm^2 have been observed by myself at 30 kv. Aritome has observed threshold currents of approximately 2.6 A/cm^2 maximum for CdS platelets pumped with a 20 kv electron beam. For the crystal used in this experiment the threshold current at 22 kv. is approximately 4.0 A/cm^2. Thus it seems that the crystal used for this experiment is a high threshold crystal relative to thresholds typically obtained by myself as well as others. These thresholds are less than the 7.0 A/cm^2 threshold obtained for a bulk CdS crystal used by Shewchun (2) or for the bulk crystals of CdSe (4). However, for the ZnO platelets of reference (5), the threshold of the CdS platelet examined here is much larger than the reported 1.8 A/cm^2 at 30 kv measured for ZnO.

WAVELENGTH TUNING OF THE STIMULATED EMISSION

Because of the short pulse mode of operation, the light emission is a function of time. There is a delay between the start of the electron pulse and the peak of the stimulated emission at a given wavelength. This delay varies linearly with wavelength at a rate of approximately 1.45 Å/ns at 22kv, .85 Å/ns at 30kv, and .65 Å/ns at 40kv, and is independent of pumping intensity. A set of photographs showing the delay in the stimulated emission pulse as wavelength is changed are shown in figure 3. Figure 4 shows a typical plot of the delay time versus wavelength for a current density of 3.6 A/cm^2 at 30 kv. Since a plot of the delay time t at the peak of the light intensity output versus wavelength shows an approximately linear relationship, a tuning rate R in Angstroms per nsec can be calculated at each pumping current density. The conditions of view for the data in figure 4 are with the monochromator aligned along the cavity axis in a plane perpendicular to a cavity face (0° condition) and the radiation sampled through a 1° slit. Figure 5 shows the variation of the tuning rate R as the current density is increased for the three beam voltages, 22, 30, and 40 kv. It will be noted that the initial increase in R to longer wavelengths with pumping current density is followed by a saturation region. This saturation region is closely related to lasing threshold at the three beam voltages. The rectangular boxes in figure 5 indicate the region of lasing threshold. These results are consistent with those noted by Garside for GaAs and CdSe (4) A comparison with the saturated tuning rate of 1.1 Å/ns at 35 kv for CdS bulk crystal with a lasing threshold of approximately 7.0 A/cm^2, measured by Shewchun (2) appears consistent with these measurements when the lower threshold

values for the platelet used here are taken into account.

Wavelength tuning rates measured on CdS platelets with thresholds between 1.0-2.0 A/cm^2 at 30 kv showed no saturation effects and were about .04 Å/ns. This rate can be compared with the rate of .14 Å/ns per 1 A/cm^2 taken at 20 kv* by Aritome which also revealed no saturation effects (1). Wavelength tuning measurements for spontaneous luminescence from CdS bulk crystals (2) gave values of .17 Å/ns at 3.9 A/cm^2 and 30 kv beam. It is also interesting to note that the ZnO platelets examined by Shewchun (5) revealed no rapid wavelength tuning for his low threshold crystal with a threshold of approximately 1.8 A/cm^2.

* Account must be taken of the beam voltage used by Aritome. Measurements taken of the CdS platelet here show the tuning rate increases dramatically as the beam voltage is lowered.

ANGULAR TUNING OF THE STIMULATED EMISSION

The emitted light in a given radial direction in the plane containing the laser axis and the electron beam path was detected by a photomultiplier tube employing a single slit aperature. The detector signal was observed through the time window of a sampling oscilloscope and recoaded on a x-y recorder. By varying the radial direction of the phototube, a plot of the light intensity versus angle for a given delay time after the start of the electron beam pulse could be obtained. Figures 6 through 13 show sets of far field radiation patterns plotted as a function of deviation angle from the cavity axis (0^o) observed at different times following the start of the pump pulse. Negative angles represent the quadrant toward the electron beam. Figures 9 and 10 in addition show the far field radiation patterns as a function of deviation angle integrated over all time. At 30 kv and 3.6 A/cm^2 the deviation angle for all time is approximately 3^o. At 40 kv and 3.2 A/cm^2 the deviation of the far field intensity pattern integrated over all time is approximately 0^o. In figures 6 through 12, the far field intensity pattern appears to be centered at approximately 0^o with several peaks appearing at different angles in time.

Figure 13 is the far field pattern for a point on the crystal where the light output followed the shape of the electron pulse rather than peaking as in figure 3. The far field pattern for the spontaneous light is quite different than the far field patterns observed for stimulated light. Figures 6 through 12 all show that angular tuning as described by Kawasaki (3) for crystals many times thicker than 10 microns does not occur.

DISCUSSION

It appears that rapid wavelength tuning of the stimulated emission occurs in crystals having a sufficiently high laser threshold. The transition to rapid wavelength tuning isn't abrupt, however, since the rapid tuning effect of the stimulated emission is superimposed on several other wavelength tuning rates such as thermal tuning and wavelength tuning due to angular tuning which are smaller in magnitude. Below the onset of rapid tuning, such non-saturation tuning effects as the thermal tuning of spontaneous emission dominate. Furthermore since rapid wavelength tuning rate appears to depend on the saturated gain i.e. the electron-hole pair density, then as this density increases until saturation so does the tuning rate. If the electron-hole pair saturation density is approximately the same for most semiconductors i.e. similar losses, then this would account for observed rapid tuning rates for various semiconductors being approximately equal (2)(4).

B. Kawasaki has hypothesized that there would be no angular deviation of the far field pattern for platelets which are thin enough to completely confine the laser spatial mode within the pumped region of the crystal. My platelet which was 10 microns thick was too thick to completely verify this supposition. However, as the beam voltage was increased, the angular deviation of the far field pattern approached zero. Instead of the deviated far field pattern swinging towards the axis as the time delay after the start of the pumping increased, the far field pattern exhibited

intensity peaks which appeared at different angles in time about the deviated angle of the far field pattern. There were several intensity peaks noted for any delay time, suggesting several spatial modes existing at the same time within the cavity. The threshold currents for these higher order modes are very similar-if the modes "fill" the cavity-and closely spaced, unlike the situation occuring in bulk crystals where only one spatial laser mode exists in the cavity.

For bulk crystals the losses due to diffraction of the near field into the unpumped region, g_{diff}, are quite large. However, for thin enough platelets where the laser spatial mode fills the cavity, g_{diff} should be quite small. If g_{diff} is very small then the variation of threshold current will not be as rapid with voltage. In a rough way, if the mode fills the platelet one might suppose that the threshold would occur at approximately fixed input energy (i.e. constant necessary number of electron-hole pairs). From figure 1,

22 kv V x i ~ 4.0 x 22 = 88

30 kv V x i ~ 3.0 x 30 = 90

40 kv V x i ~ 2.0 x 40 = 80

where V is the beam voltage, and i is the current density. The approximately constant energy numbers support the idea of g_{diff} small and the mode "fills" the platelet.

The spatial mode assumed by Kawasaki for a semi-infinite crystal is not applicable to thin platelets. The laser spatial mode was calculated for CdS assuming a semi-infinite crystal and the value of the amplitude at 10 microns from the surface was noted to see if it were significant.

The results of the calculation are plotted in figures 14, 15 and 16 for various index step values. The index step changes were calculated using data for the variation of index step with temperature (6) and temperature profile curves shown in figure 17. The sources of refractive index and thermal parameters are given with figure 17. Figures 14, 15 and 16 show that even for large index step changes corresponding to extremely large temperature increases between the pumped and unpumped region, the amplitude of the laser spatial mode is still quite large at 10 microns. The equation for the spatial mode of (3) probably over-estimates the gain at $x = d$ since the gain should decrease smoothly across this region. For this reason the calculation was repeated using Bogdankevich's "sech^2" model for the spatial mode. Figures 18, 19 and 20 show the spatial modes for various index changes. Bogdankevich's model tends to underestimate the gain at $x = d$ for two reasons. Firstly, the "sech^2" model is parametrized to be equivalent in half-height width of gain to the truncated gaussian shape of differential energy loss (dE/dx) of the electron beam (8). The gain shape thus does not reflect the profile broadening effects of gain saturation. Secondly, this model also lacks the profile broadening which would be caused by carrier diffusion. This model does, however, include a tailing-off of gain toward the unpumped region, in direct contrast to the model of (3).

The actual spatial mode lies somewhere between these two models for a semi-infinite crystal. In any case the modes as calculated by Bogdankevich and Kawasaki assuming a semi-infinite crystal always sees the far face of the platelet for small index changes and their corresponding temperature changes between the

pumped and unpumped regions. Thus spatial modes derived from semi-infinite crystal models are inapplicable to platelets of this thickness and the angular results for the platelet used in this experiment can not be completely explained using Kawasaki's and Bogdankevich's models. Instead the laser spatial mode within the platelet must be solved for.

REFERENCES

1. H. Aritome, K. Masuda and S. Namba, IEEE J. Quantum Electron. QE-7 118 (1971).

2.0 J. Shewchun, B. Kawasaki, B. Garside, IEEE J. Quantum Electron. QE-6 113 (1970).

3.0 B. Kawasaki, PhD Thesis, McMaster University, August 1972.

4.0 B. Garside, J. Shewchun, and B. Kawasaki, IEEE J. Quantum Electron. QE-7 88 (1971).

5.0 J. Shewchun, B. Garside, B. Kawasaki, T. Efthymiopoulos J. of Applied Physics Vol. 43 2 pp545 (1972).

6.0 D. Langer, J. of Applied Physics Vo. 37 Number 7 pp 3530 (1966).

7.0 A. Ashkin, B. Tell, J. Dziedzic, IEEE J. Quantum Electon. QE-3 pp 400 (1967).

8.0 C. Klein, Applied Optics Vol. 5 12 (1966).

9.0 O.V. Bogdankevich, V. Letokhov, A. Suchkov, Soviet Physics - Semiconductors Vol. 3 Number 5 pp 566 (1969).

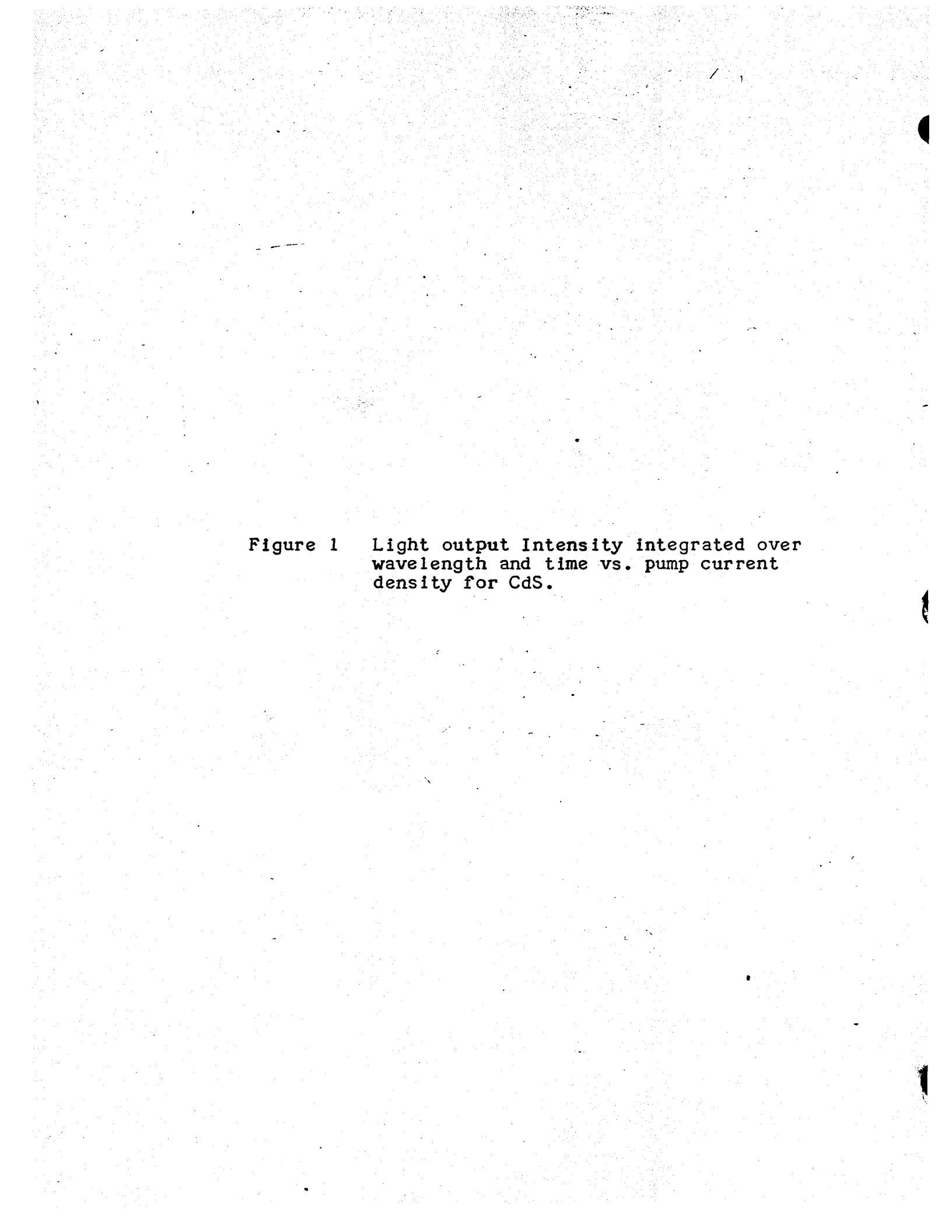

Figure 1 Light output Intensity integrated over wavelength and time vs. pump current density for CdS.

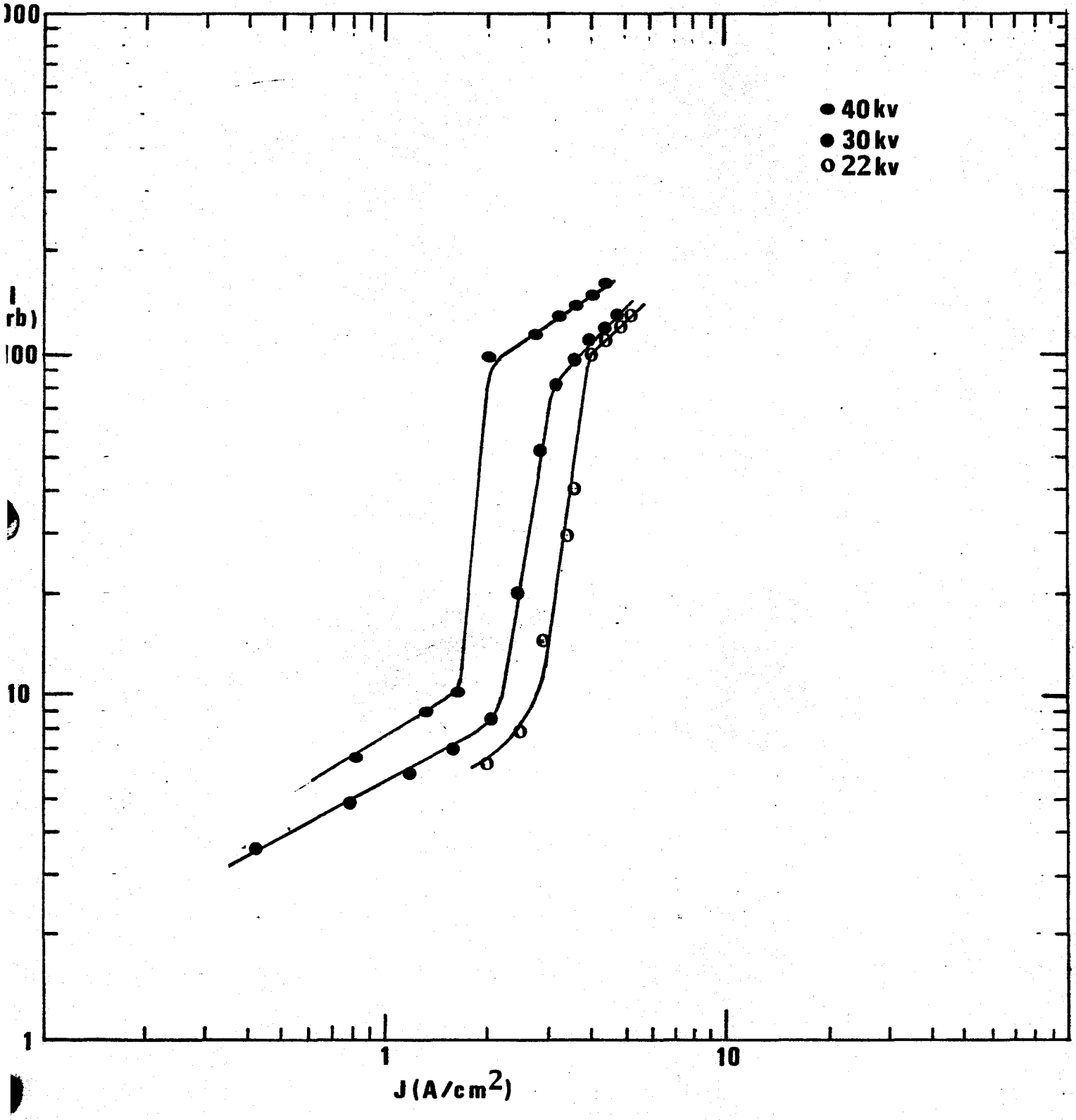
)00
I
rb)
100
10
1
1
10
J(A/cm2)
40kv
30kv
22kv

Figure 2 Mode spectra integrated over all time for beam voltage of 30 kv. The dewar temperature is 77°K.

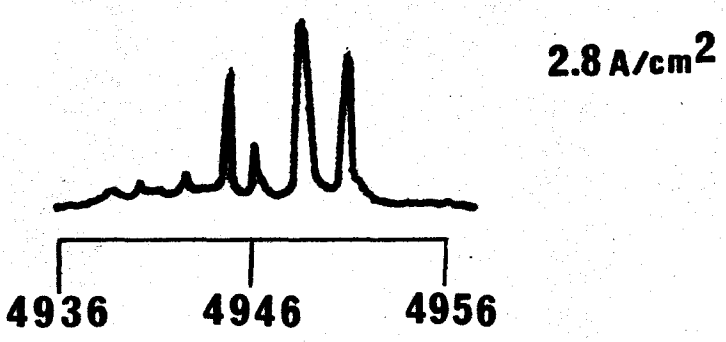
2.8 A/cm2
4936
4946
4956

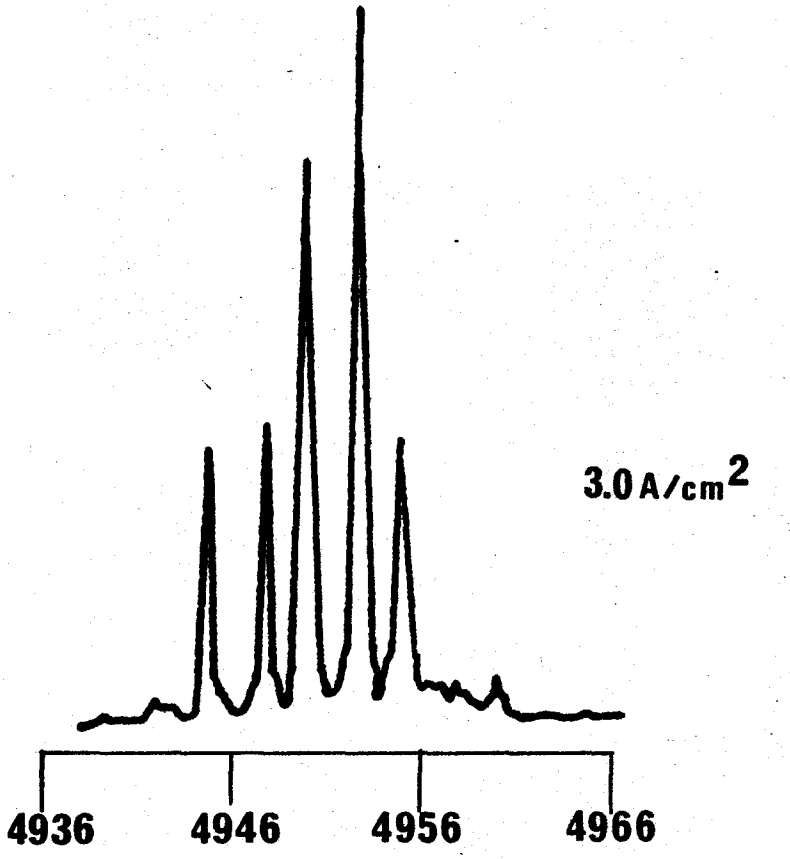
3.0 A/cm2
4936
4946
4956
4966

Figure 3 Delay shift as wavelength is changed. Current density 3.2 A/cm^2, Beam voltage 40 kv. Time base is 20 ns/div.

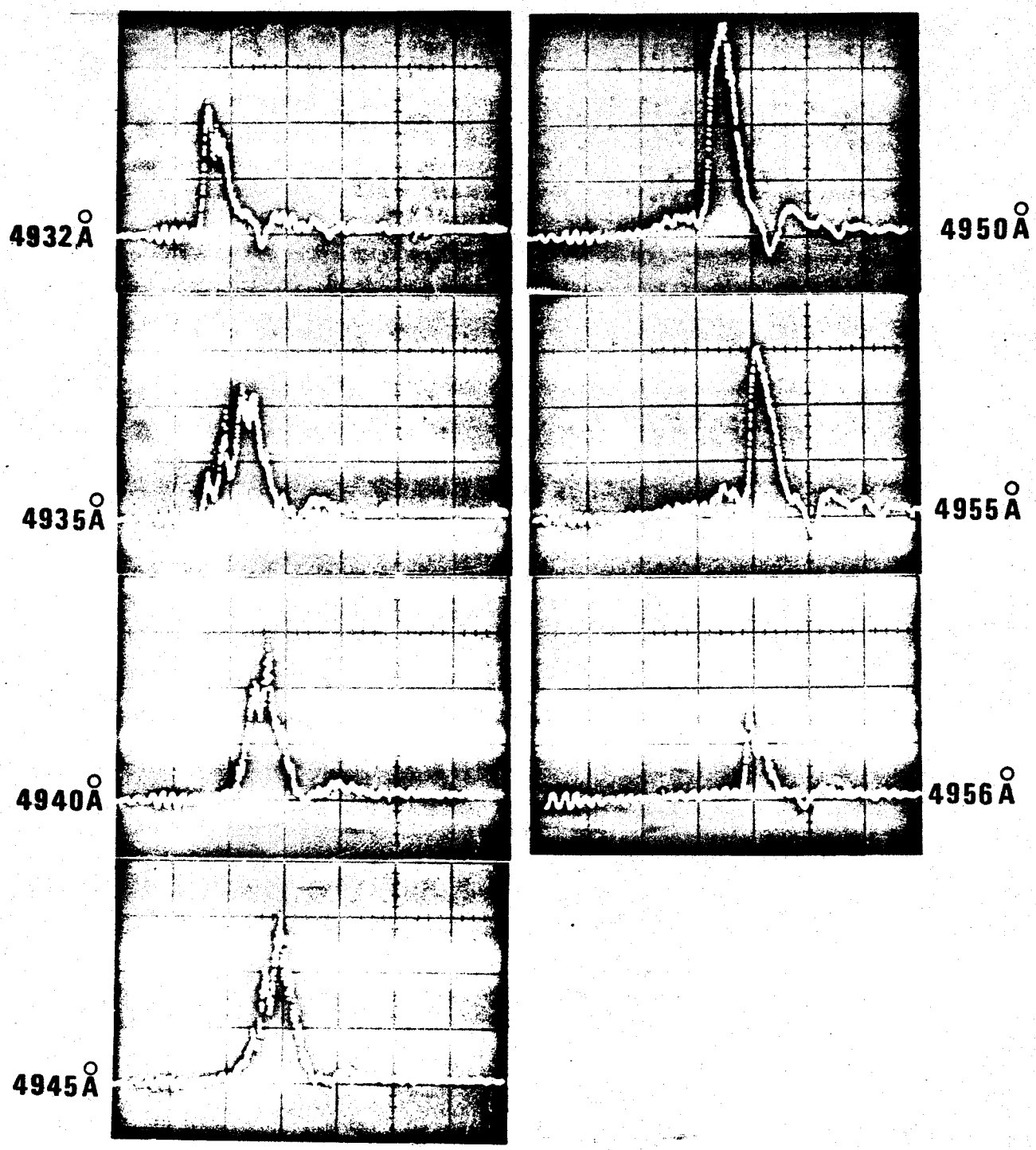
4932Å
4935Å
4940Å
4945Å
4950Å
4955Å
4956Å

Figure 4 Plot of delay time versus wavelength for a beam voltage of 30 kv at a current of 3.6 A/cm2.

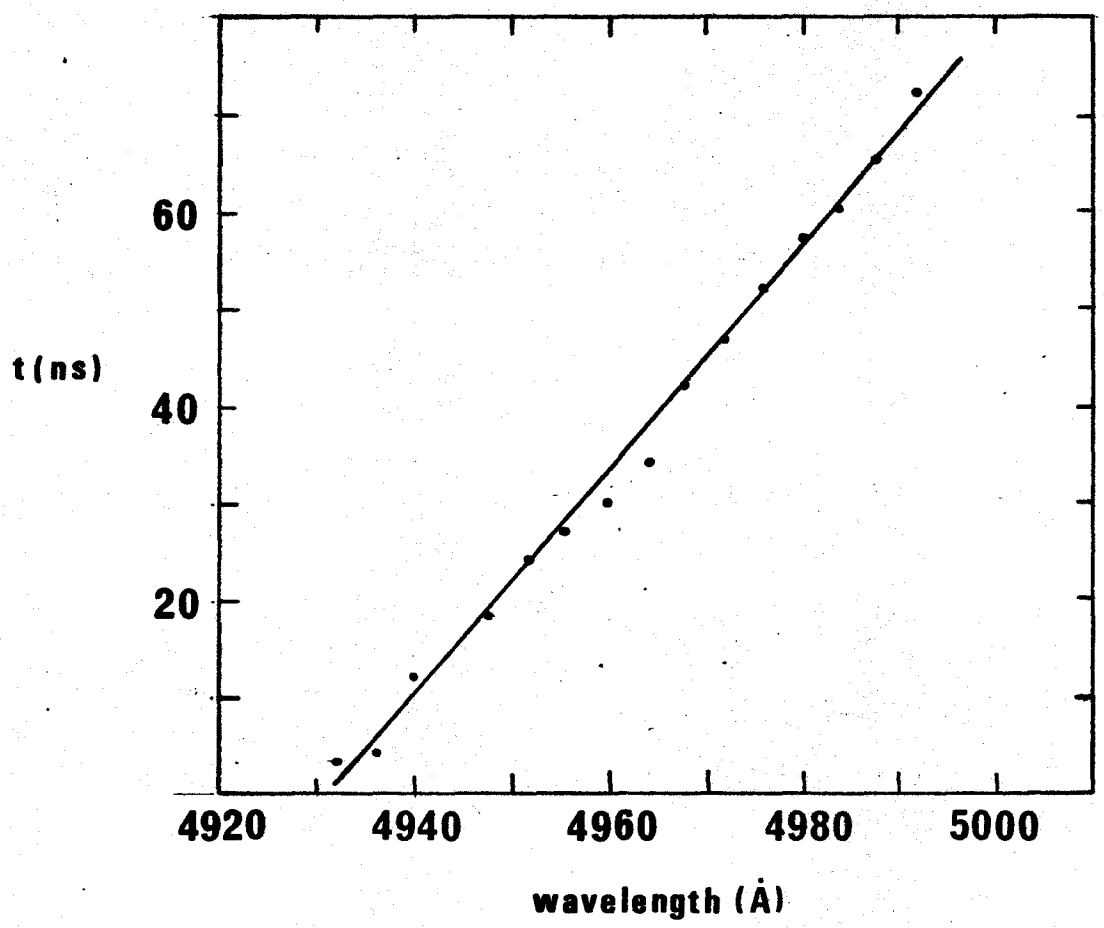
t(ns)
60
40
20
4920
4940
4960
4980
5000
wavelength (Å)

Figure 5 Plot of the tuning rate R to longer wavelengths against pumping current density. Temperature is 77°K. Conditions of view are 0° with a 1° slit. The rectangular boxes indicate the ranges of laser threshold - current density.

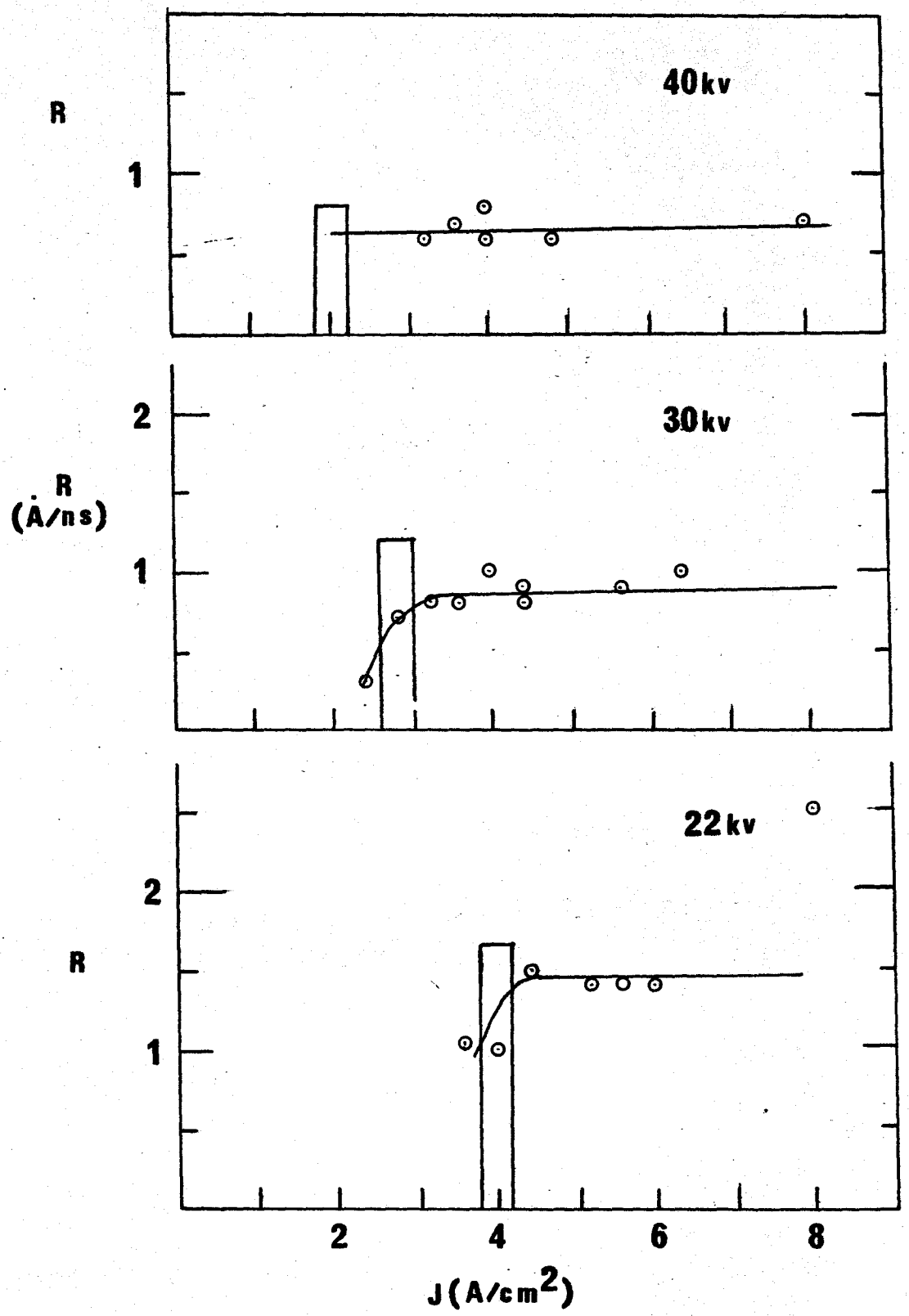
40kv
30kv
22kv
R
R
(A/ns)
R
1
2
1
2
1
2
4
6
8
J(A/cm2)

Figure 6 Far field radiation pattern at various times after the start of the pulse.

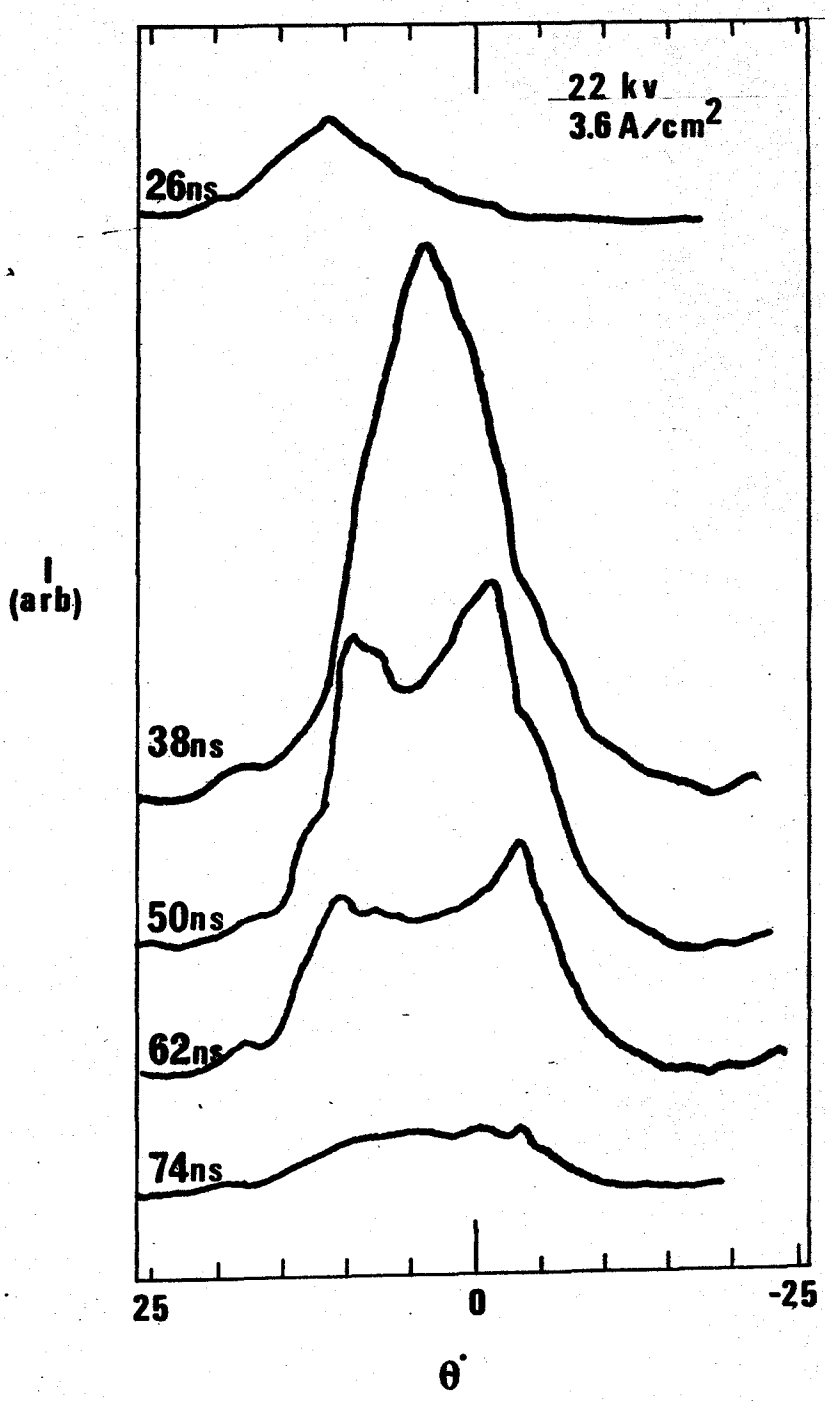
22 kv
3.6 A/cm²
26ns
38ns
50ns
62ns
74ns
I
(arb)
25
0
-25
θ°

Figure 7 Far field radiation pattern at various times after the start of the pulse.

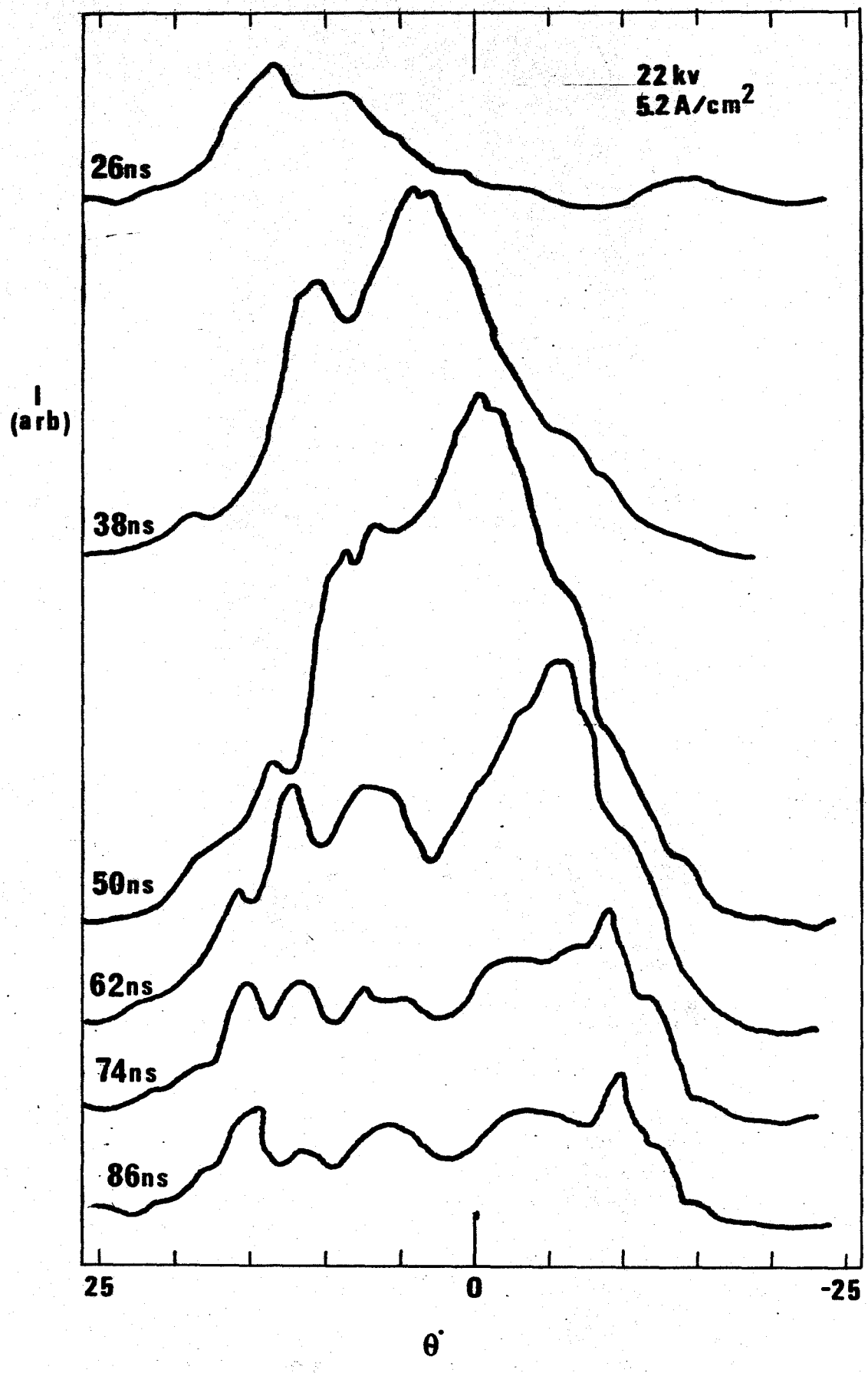
22 kv
5.2 A/cm2
26ns
38ns
50ns
62ns
74ns
86ns
I
(arb)
25
0
-25
θ°

Figure 8 Far field radiation pattern at various times after the start of the pulse.

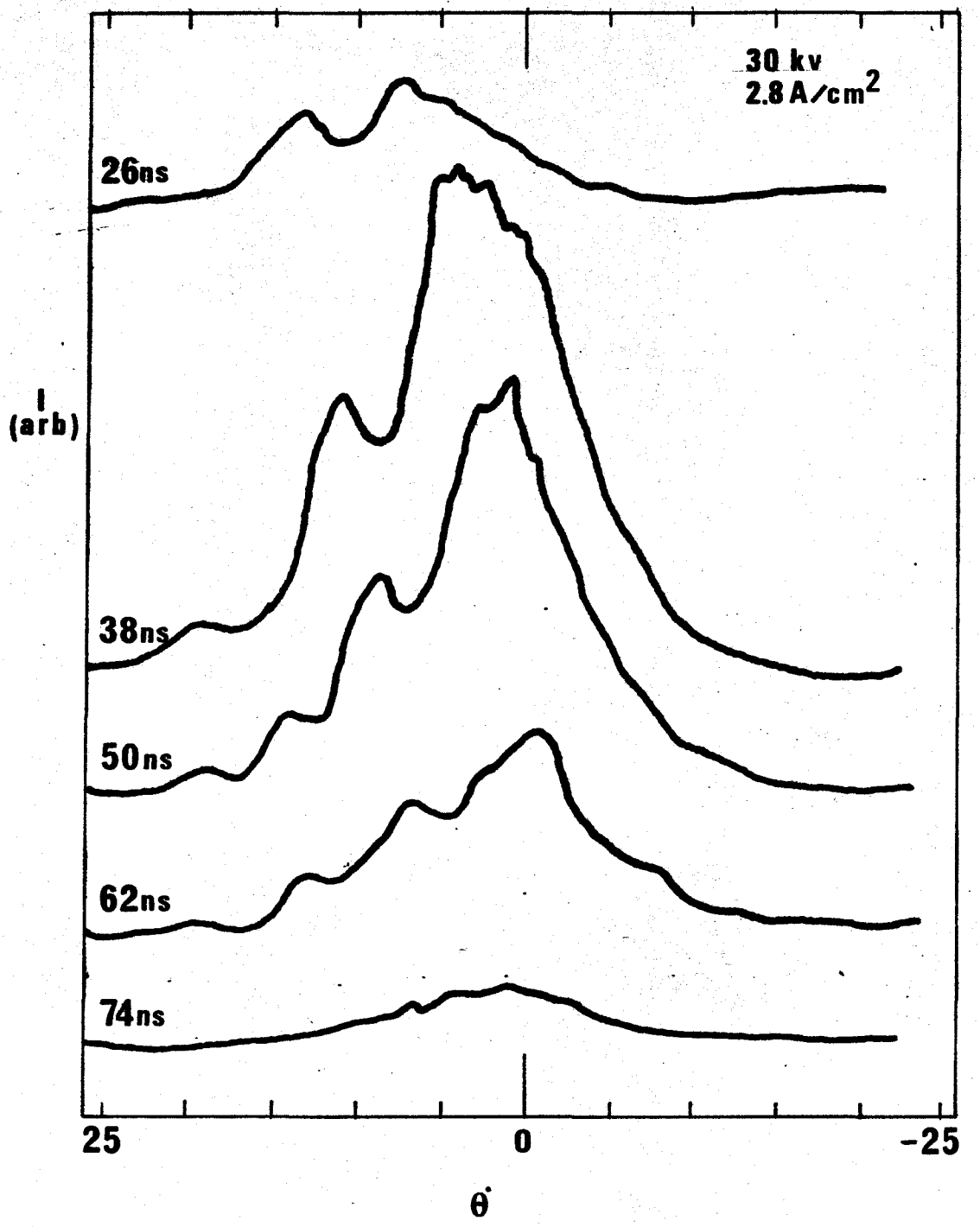
30 kv
2.8 A/cm2
26ns
38ns
50ns
62ns
74ns
I
(arb)
25
0
-25
θ°

Figure 9 Far field radiation pattern at various times after the start of the pulse.

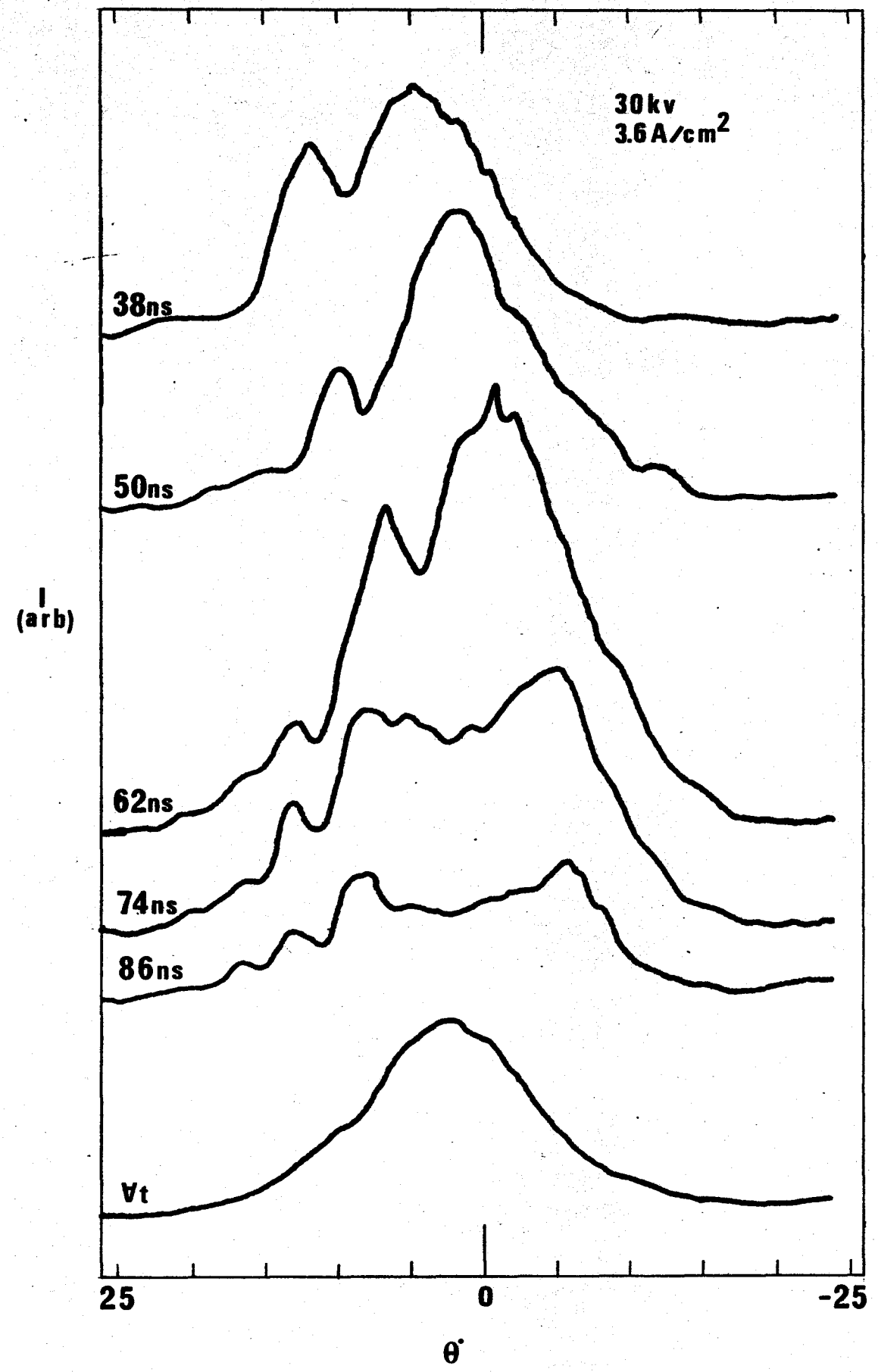
30kv
3.6A/cm2
38ns
50ns
62ns
74ns
86ns
∀t
I
(arb)
25
0
-25
θ°

Figure 10 Far field radiation pattern at various times after the start of the pulse.

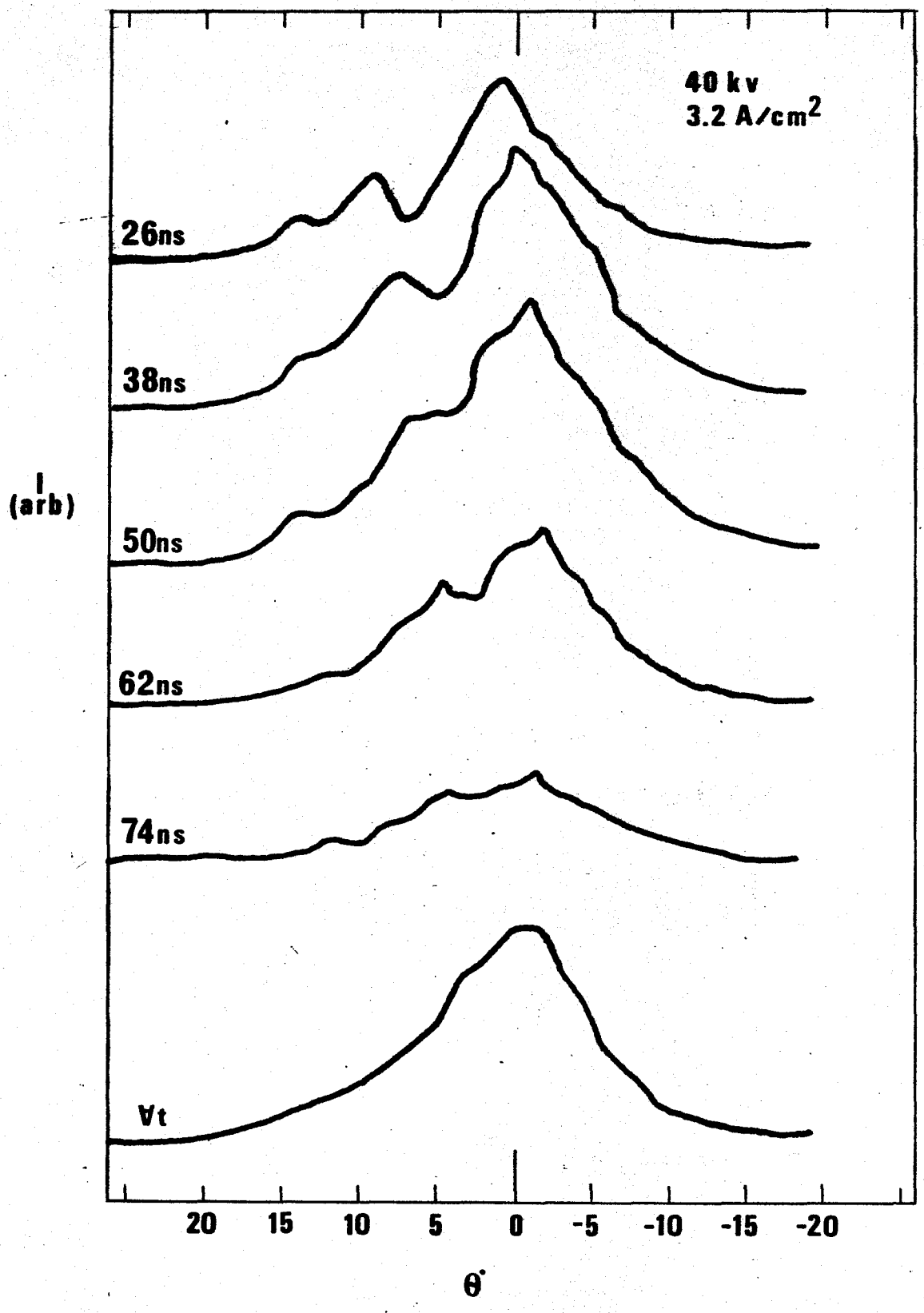
40 kv
3.2 A/cm2
26ns
38ns
50ns
62ns
74ns
Vt
I
(arb)
20
15
10
5
0
-5
-10
-15
-20
θ°

Figure 11 Far field radiation pattern at various times after the start of the pulse.

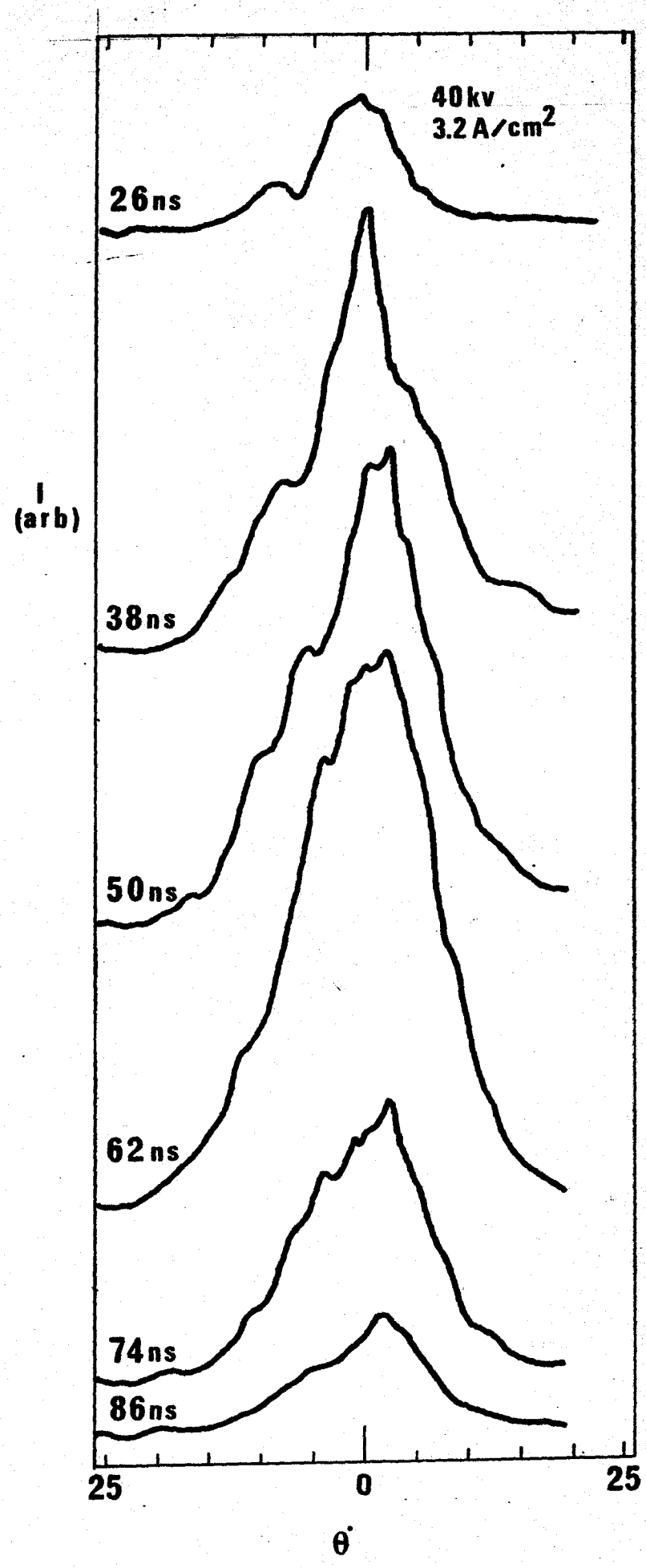
40kv
3.2 A/cm²
26ns
38ns
50ns
62ns
74ns
86ns
I
(arb)
25
0
25
θ°

Figure 12 Far field radiation pattern at various times after the start of the pulse.

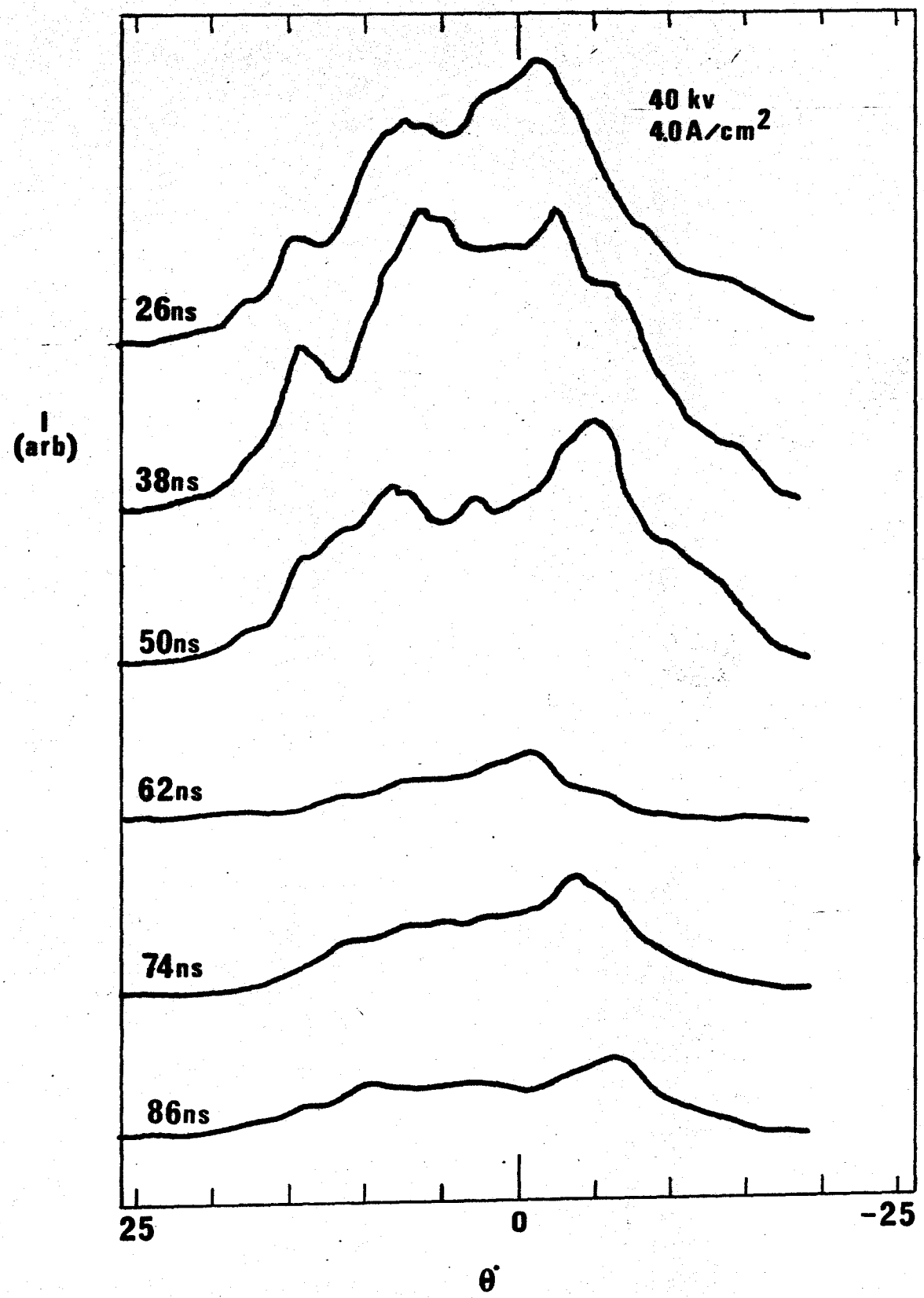
40 kv
4.0 A/cm²
26ns
38ns
50ns
62ns
74ns
86ns
I
(arb)
25
0
-25
θ°

Figure 13 Far field radiation pattern at various times after the start of the pulse for spontaneous light.

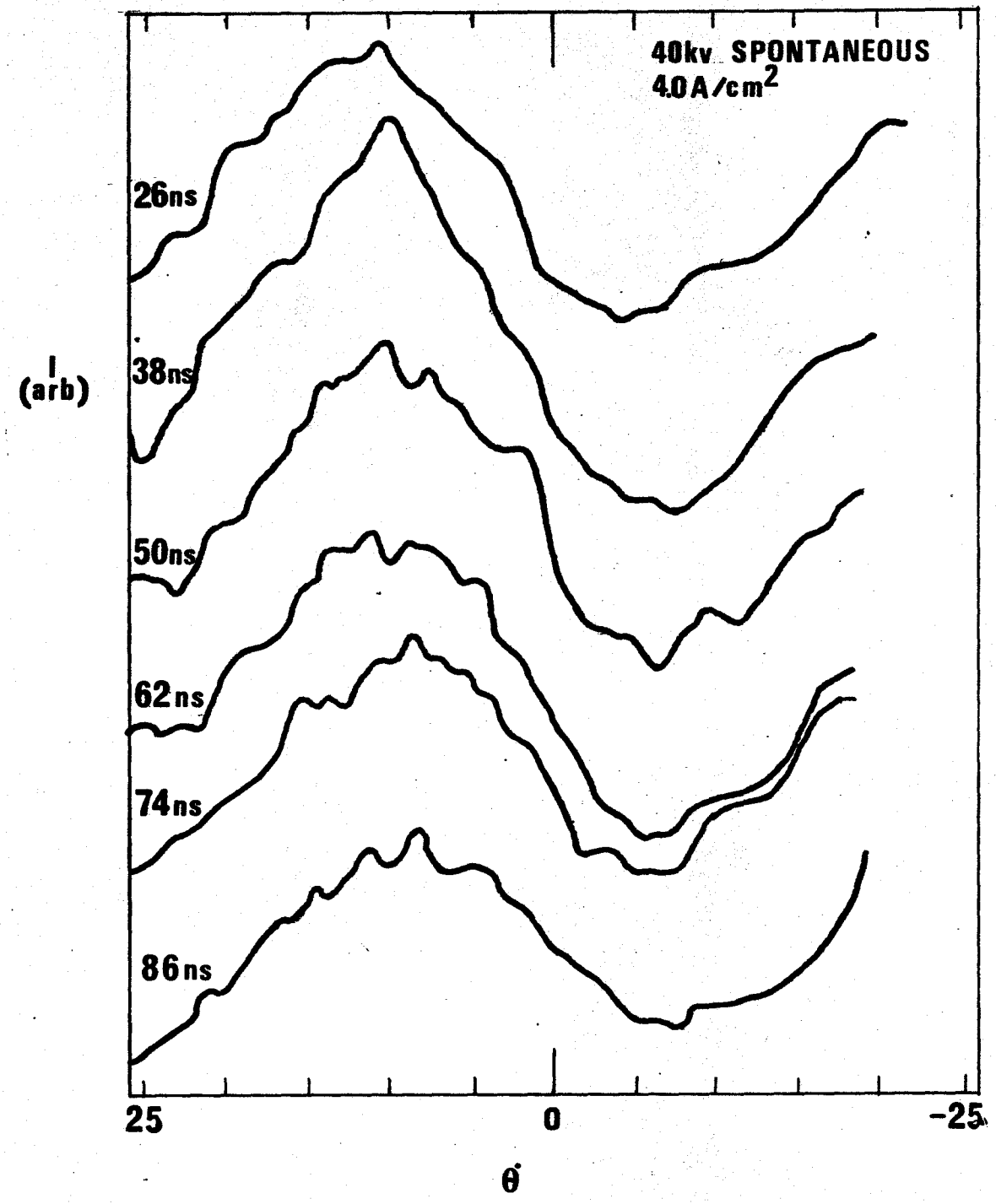
40kv SPONTANEOUS
4.0A/cm2
26ns
38ns
50ns
62ns
74ns
86ns
I
(arb)
25
0
-25
θ

Figure 14 Spatial mode calculated from Kawasaki's semi-infinite crystal model. The solid lines represents the depth of the pumped region. a_s = 13 cm-1(7) Beam voltage 22kv. Realistic temperature rise lies between 3°K to 25°K (depending on pumping current density) as obtained from temperature profiles like those in figure 17.

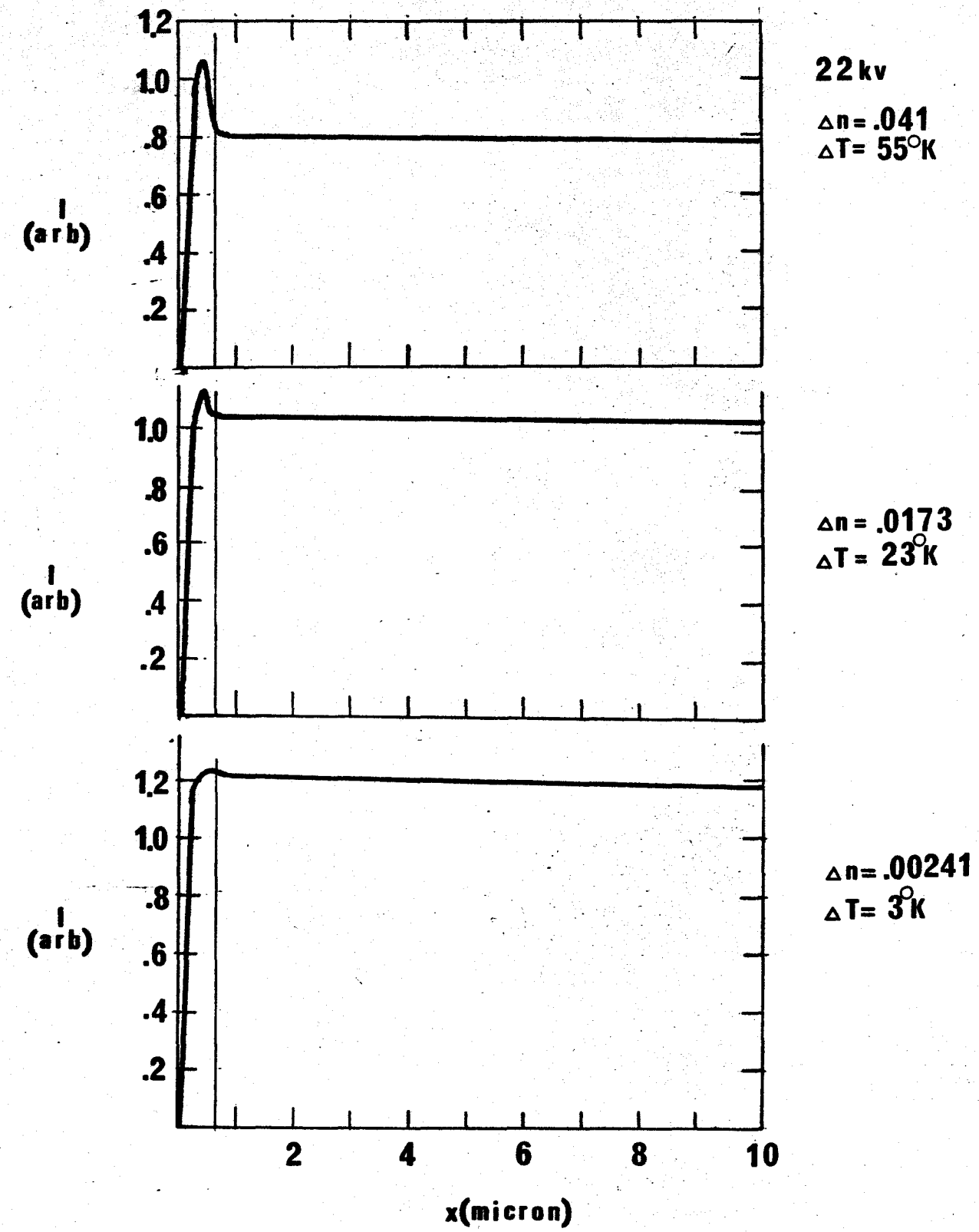
1.2
1.0
.8
.6
.4
.2
I (arb)
22 kv
Δn = .041
ΔT = 55°K
1.0
.8
.6
.4
.2
I (arb)
Δn = .0173
ΔT = 23°K
1.2
1.0
.8
.6
.4
.2
I (arb)
Δn = .00241
ΔT = 3°K
2
4
6
8
10
x(micron)

Figure 15 Spatial mode calculated from Kawasaki's semi-infinite crystal model. The solid lines represents the depth of the pumped region. a_s = 13 cm-1 Beam voltate 30 kv. Realistic temperature rise lies between 3°K to 25°K (depending on pumping current density) as obtained from temperature profiles like those in figure 17.

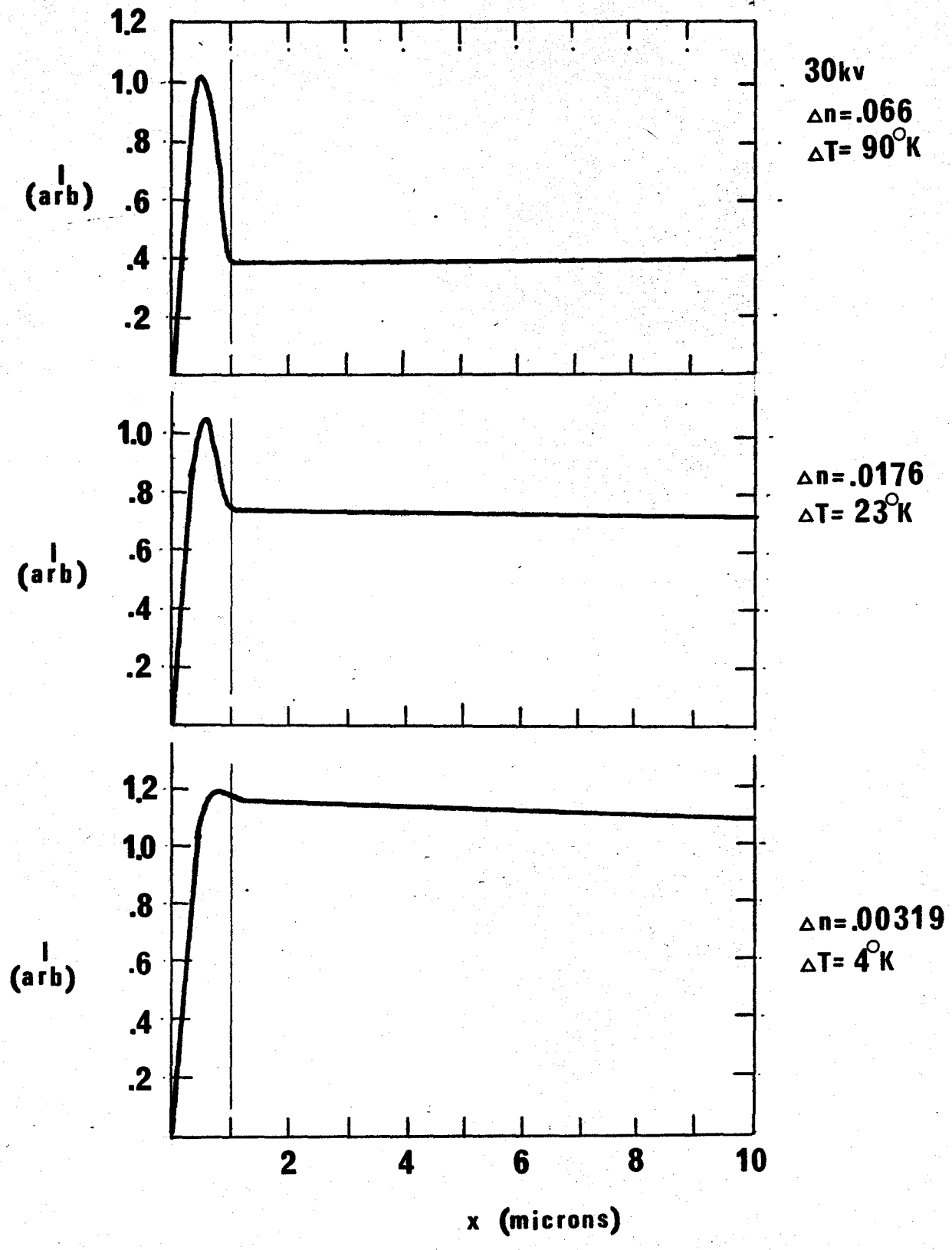
1.2
1.0
.8
.6
.4
.2
I (arb)
30kv
Δn=.066
ΔT= 90°K
Δn=.0176
ΔT= 23°K
Δn=.00319
ΔT= 4°K
2
4
6
8
10
x (microns)

Figure 16 Spatial mode calculated from Kawasaki's semi-infinite crystal model. The solid lines represents the depth of the pumped region. a_s = 13cm-1 Beam voltage is 40 kv. Realistic temperature rise lies between 3°K to 25°K (depending on pumping current density) as obtained from temperature profiles like those in figure 17.

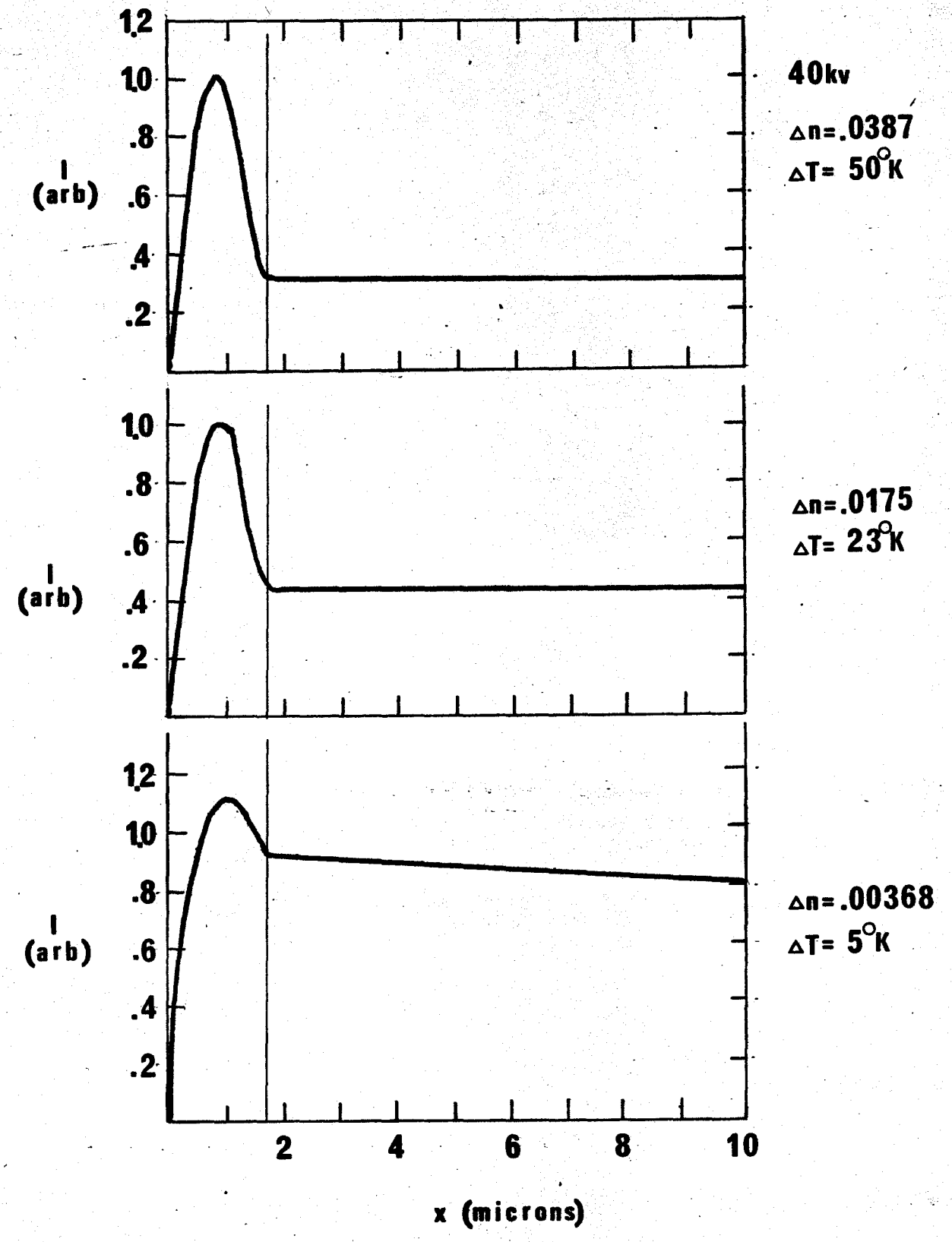
1.2
1.0
.8
.6
.4
.2
I (arb)
40kv
Δn=.0387
ΔT= 50°K
1.0
.8
.6
.4
.2
I (arb)
Δn=.0175
ΔT= 23°K
1.2
1.0
.8
.6
.4
.2
I (arb)
Δn=.00368
ΔT= 5°K
2
4
6
8
10
x (microns)

Figure 17 Calculated temperature profiles of beam-pumped CdS at an initial temperature of 77°K. (The plots are in 40 ns steps). Thermal diffusivity = .636 cm^2/sec, thermal conductivity = 1 w/cm^oK, specific heat = .078 cal/gm^oK, density = 4.82 gm/cm^3. Equation for calculation obtained from (3). The straight lines indicate the depth of the pumping region. These depths have been calculated from (8). Refractive index data from (6).

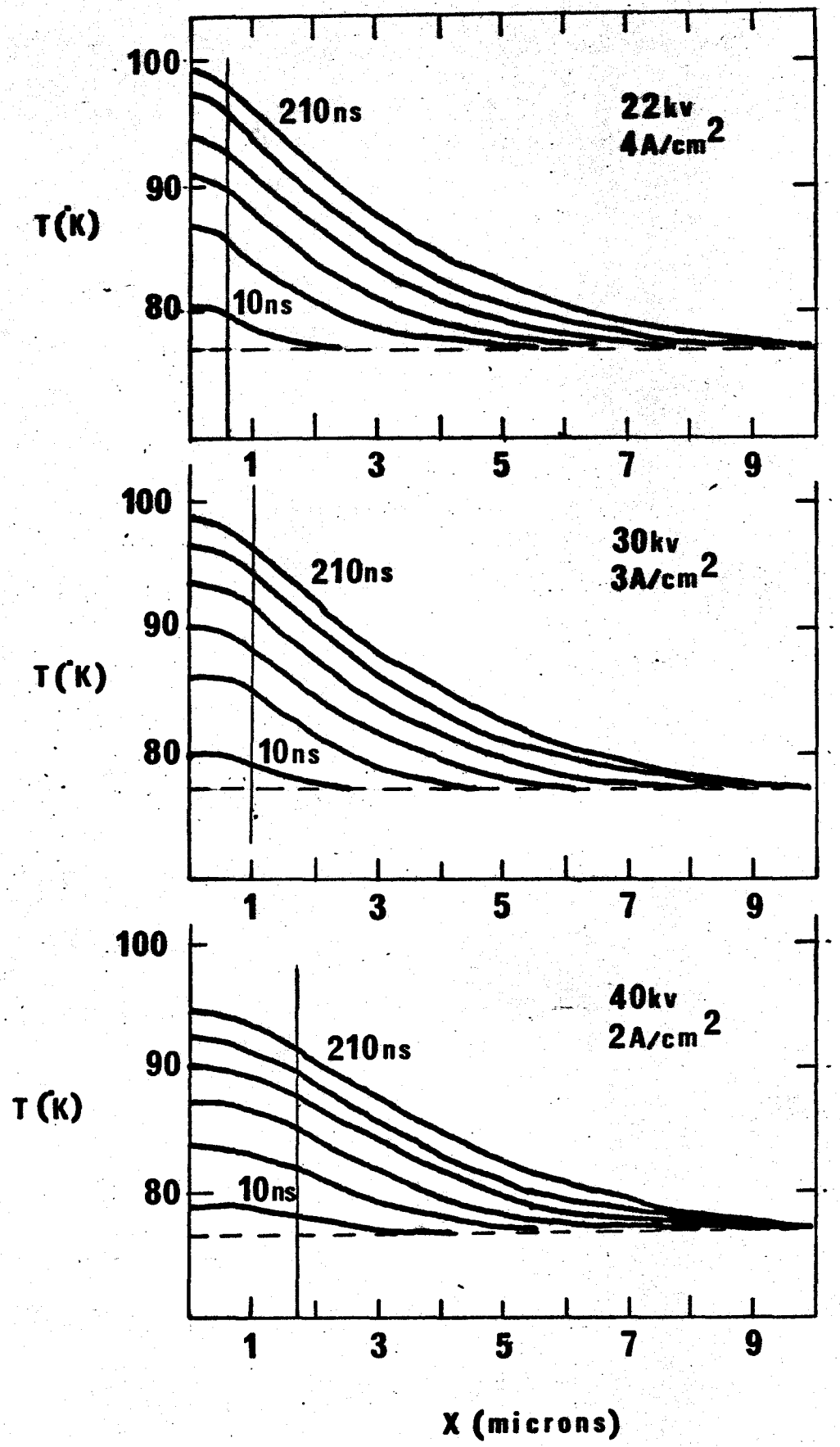
100
90
80
T(K)
210ns
10ns
22kv
4A/cm2
1
3
5
7
9
30kv
3A/cm2
40kv
2A/cm2
X (microns)

Figure 18 Spatial mode calculated from Bogdankevich's semi-infinite crystal model. The solid lines represents the depth of the pumped region. a_s = 13 cm-1(7) Beam voltage 22kv. d = .6 microns.

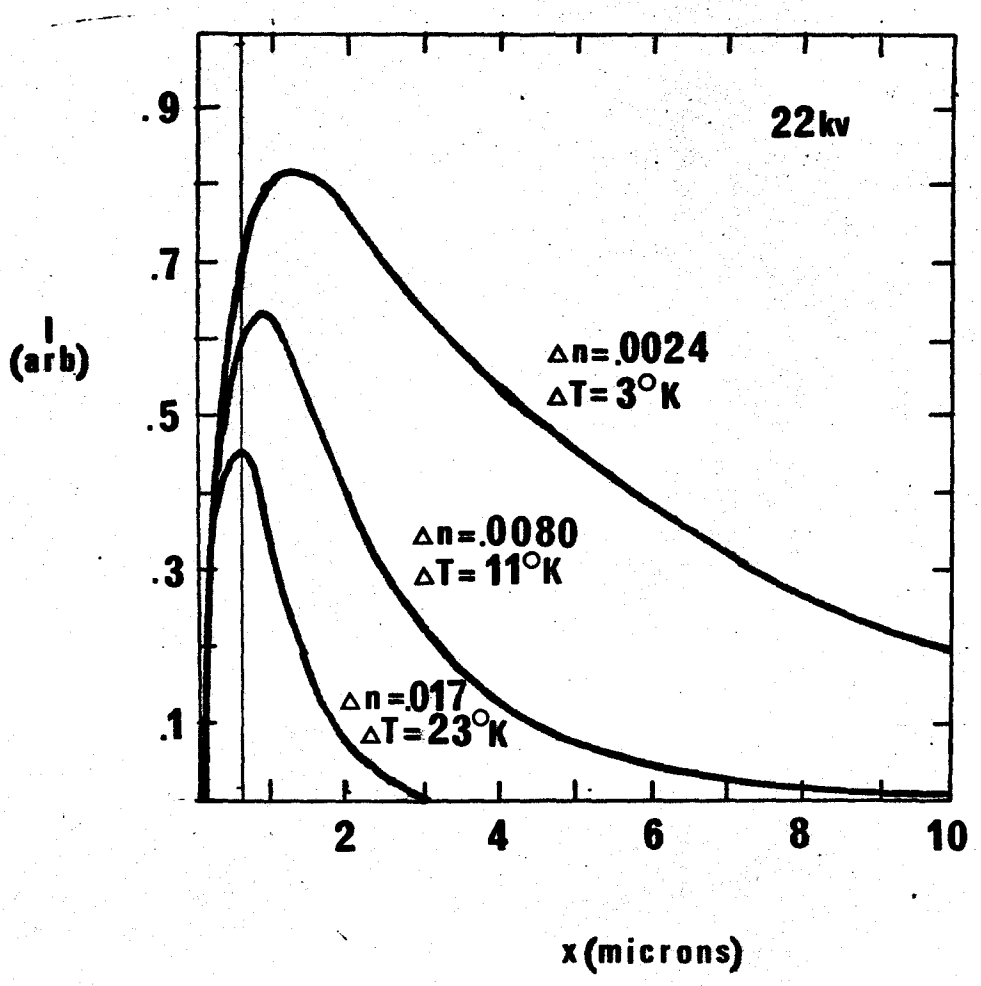
22kv
.9
.7
.5
.3
.1
I (arb)
Δn=.0024
ΔT=3°K
Δn=.0080
ΔT=11°K
Δn=.017
ΔT=23°K
2
4
6
8
10
x (microns)

Figure 19 Spatial mode calculated from Bogdankevich's semi-infinite crystal model. The solid lines represents the depth of the pumped region. a_s = 13 cm-1(7) Beam voltage 30 kv. d = 1.0 microns.

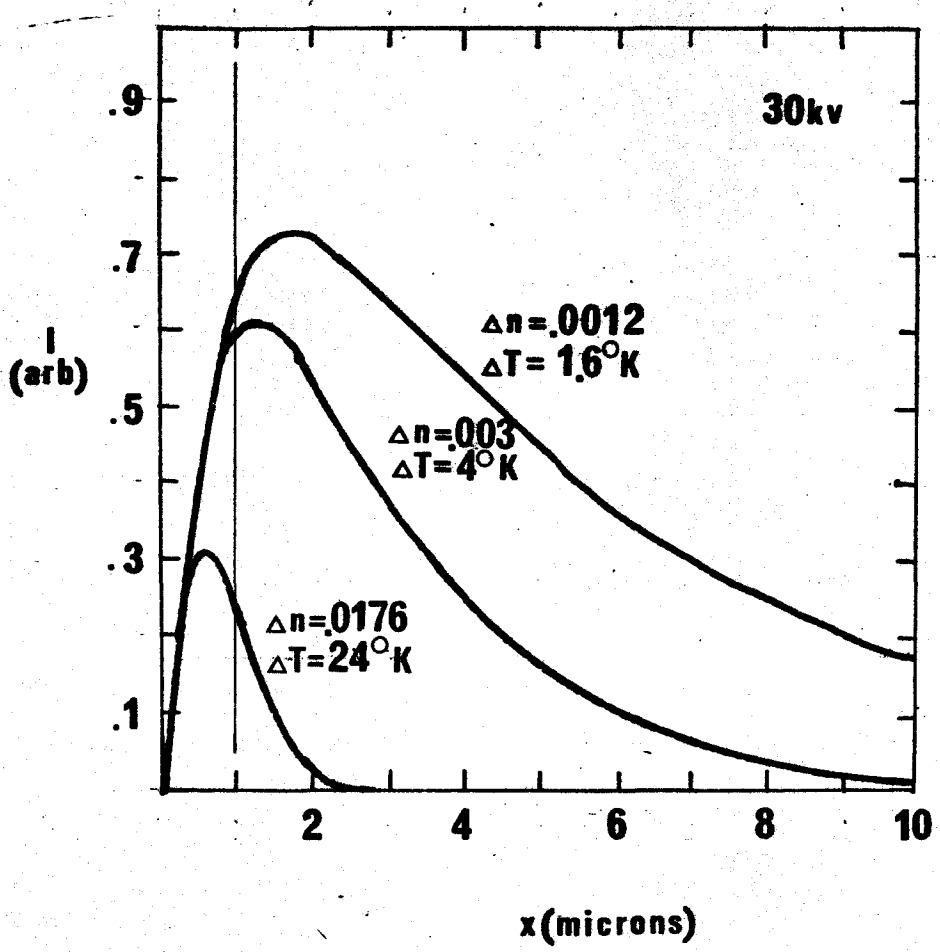
30kv
.9
.7
.5
.3
.1
I
(arb)
Δn=.0012
ΔT= 1.6°K
Δn=.003
ΔT=4°K
Δn=.0176
ΔT=24°K
2
4
6
8
10
x(microns)

Figure 20 Spatial mode calculated from Bogdankevich's semi-infinite crystal model. The solid lines represents the depth of the pumped region. a_s = 13 cm-1(7) Beam voltage 40 kv. d = 1.7 microns.

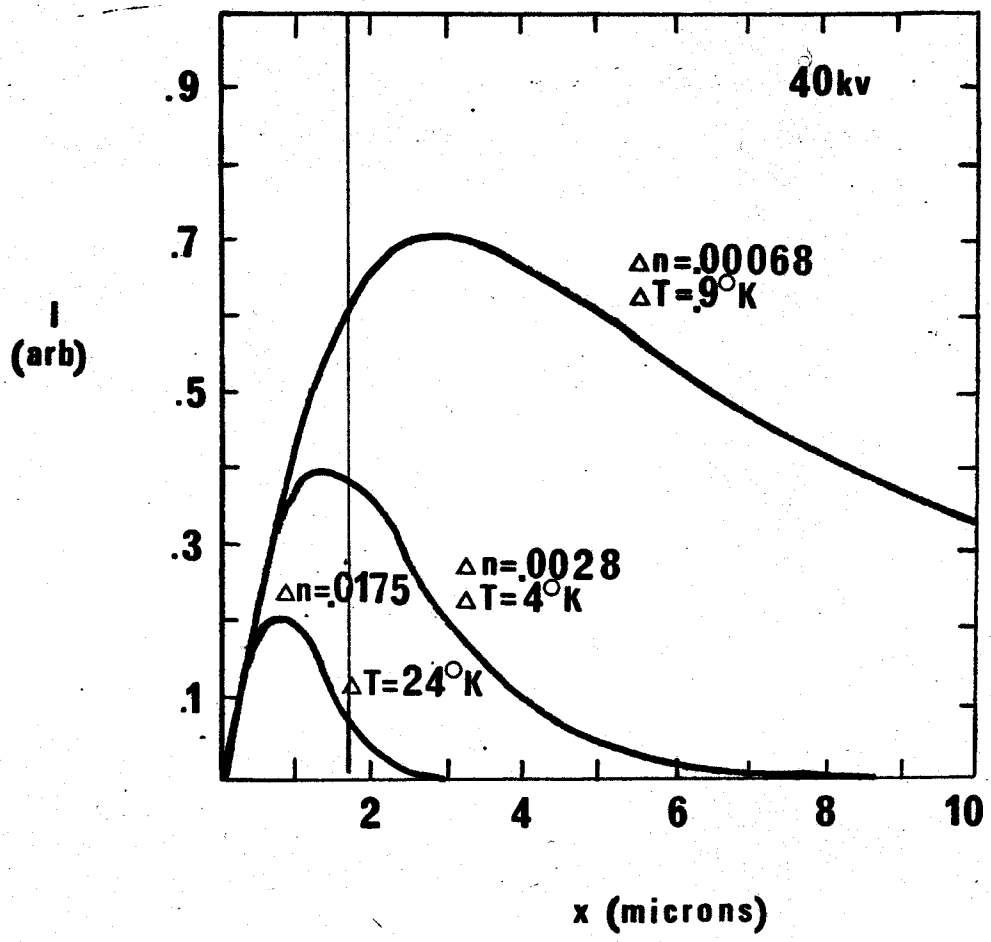
40kv
.9
.7
.5
.3
.1
I
(arb)
Δn=.00068
ΔT=9°K
Δn=.0028
ΔT=4°K
Δn=.0175
ΔT=24°K
2
4
6
8
10
x (microns)